TEN-YEAR ANALYSIS OF TROPOPAUSE-OVERSHOOTING CONVECTION OVER THE EASTERN UNITED STATES USING NEXRAD DATA

A Thesis

by

JOHN WILLIAM COONEY

Submitted to the Office of Graduate and Professional Studies of
Texas A&M University
in partial fulfillment of the requirements for the degree of

MASTER OF SCIENCE

Chair of Committee,	Kenneth Bowman
Committee Members,	Christopher Nowotarski
	David Brooks
	Kenneth Bowman
Head of Department,	Ping Yang

December 2016

Major Subject: Atmospheric Sciences

ABSTRACT

Mass-exchange across the tropopause can have a substantial impact on the composition, radiation, and chemistry of the Upper Troposphere and Lower Stratosphere (UTLS). Convection that penetrates the tropopause (overshooting convection) can rapidly transport air from the lower troposphere to the lower stratosphere and can potentially mix stratospheric air into the upper troposphere. To improve our understanding of overshooting convection, this study conducts a 10-year statistical analysis of overshooting convection for the May-August period of 2004 to 2013 over the continental United States, east of the Rocky Mountains. Using 104 radars from the National Oceanic and Atmospheric Administration Next Generation Weather Radar (NEXRAD) network, echo-top altitudes are derived from radar reflectivities that are merged into hourly, high-resolution, three-dimensional, gridded synoptic analyses. Echo-top altitudes are then compared to lapse-rate tropopause heights calculated from the European Center for Medium-Range Weather Forecasting ERA-Interim reanalysis to determine the frequency, timing, magnitude, location, and interannual variability of overshooting convection. The results of this study are obtained from analyzing only the 'storms' identified to protrude at least 2 km into the lower stratosphere.

Overshooting convection is most common in the high plains of the United States, with a weak secondary maximum observed along the east coast. There is a strong diurnal cycle with maximum overshooting occurring consistently between 2200 and 0200 UTC (late afternoon to early evening local time). The number of events per year varies by about a factor of two with 2011 having the most and 2005, the least. The total overshooting volume for each year follows a similar pattern as the occurrences. The tropopause height is found to play an important role in controlling overshooting. There are more overshooting

events observed in May and June when the tropopause height is low than in July and August. The highest number of overshooting storms have echo-top heights ranging from 15 km in May to 18 km in August. The number of storm occurrences also decreases exponentially with height above the tropopause and none are observed to extend over 8 km into the stratosphere. In this study, over 70% of individual overshooting storms have echo-tops with potential temperature values at or above 380 K, suggesting that the impact of overshooting over the United States could extend beyond the mid-latitudes and potentially into the tropical lower stratosphere.

TABLE OF CONTENTS

Page

LIST OF FIGURES

LIST OF TABLES

TABLE Page

1. INTRODUCTION AND BACKGROUND

Deep convective storms contain thermally-driven updrafts that rapidly lift boundary layer and lower tropospheric air into the Upper Troposphere and Lower Stratosphere (UTLS). Deep convection occurs around the globe, but in the extratropics in particular it has the ability to penetrate through the tropopause into the lower stratosphere (Wang, 2003; Homeyer and Bowman, 2013), where mass exchange of trace constituents can have a significant impact on composition (Dessler and Sherwood, 2004). In the UTLS, trace gases have a major impact, both directly and indirectly, on chemistry, dynamics, and radiation (Holton et al., 1995; Stohl et al., 2003; Gettelman et al., 2011). Many radiatively and chemically important species have long lifetimes in the UTLS, so their distribution is predominantly determined by transport processes. Most previous studies of transport in the UTLS focus primarily on large-scale processes, such as Rossby wavebreaking and the Brewer-Dobson circulation but transport across the tropopause by smaller scale processes is largely unknown. Determining the importance of transport by small scale processes, including convection, is vital for understanding how air is exchanged between the troposphere and stratosphere, as well as how changes in the composition and structure of the UTLS could affect the stratosphere and Earth's climate in the future.

Model simulations have been used to quantify the role of convection in Stratosphere-Troposphere Exchanges (STE) demonstrating that mass exchange across the tropopause plays a significant role on the composition and chemistry of the UTLS (Chagnon and Gray, 2010). These studies typically focus on an individual convective event or a series of convective events that occur during a field campaign and can provide insight into the importance of transport by deep convection. The studies are, however, limited in their applicability because they are unable to assess the frequency and distribution of tropopause-

penetrating events, which is necessary for a full quantitative picture of STE. Gray (2003) performs forecasts of a case study using the Met Office Unified Model with an idealized passive tracer to evaluate extratropical cross-tropopause transport and assess the quality of the results obtained by models. This study reveals model-based methods underestimate the mass-exchange across the tropopause.

Observational studies using satellite data have also been previously carried out to assess the role deep convection plays in STE. These studies can be very useful but are limited by the information that can be obtained from orbiting sensors. For example, (Berendes et al., 2008; Lindsey and Grasso, 2008; Rosenfeld et al., 2008) detect tropopause-penetrating convection through different techniques using visible or near-infrared texture and reflectance. These techniques perform well at certain times but often deteriorate from enhanced texture at large solar zenith angles associated with the diurnal cycle (Bedka et al., 2010). Bedka et al. (2010) finds that approximately 60%-75% of overshooting events occur at night over the Great Plains and western Great Lakes region and are missed by daytime-only algorithms.

Recognizing these limitations, Bedka et al. (2010) attempts to overcome them by combining a Global Forecast System (GFS) and infrared brightness temperature spatial gradients in a 5-year climatology of overshooting convection in the United States. In this study, tropopause-overshooting convection is determined by comparing, at each location, the calculated Numerical Weather Prediction (NWP) tropopause temperature with pixels where the brightness temperature is at or below 215 K. In addition, Bedka et al. (2010) requires overshooting features to be 6.5 K colder than the surrounding anvil temperatures. This technique is able to identify storms missed by day-time only algorithms and works well in most cases, however, it encounters some limitations of its own. Because overshooting height is inferred from temperature profiles, which are dependent on lapse rate conditions, the infrared window (IRW)-texture method has a false-alarm rate that ranges from 4.2% to

38.8%, depending upon the magnitude of the overshooting and algorithm quality control settings (Bedka et al., 2010).

Regardless of shortcomings in the modeling and satellite approaches, both repeatedly demonstrate that deep convection has the potential to greatly influence processes in the UTLS. In order to better understand convection, several studies merge observations from multiple radars in the Next Generation Weather Radar network (NEXRAD) into three-dimensional Cartesian grids (typically longitude, latitude, and altitude). Individual scans are combined using a variety of selection and averaging algorithms, often involving range weighting of the observations to account for systematic variations in the spatial resolution of the beam (Homeyer, 2014). This reduces storage requirements and makes the data easier to use (e.g., Zhang et al., 2005, 2011; Lakshmanan et al., 2006; Langston et al., 2007; Ruzanski and Chandrasekar, 2012). These analyses, however, have forgone important information about the vertical profile of reflectivity by interpolating to a coarse ($>$3 km) vertical grid. Homeyer (2014) and Homeyer and Kumjian (2014) show that information about the vertical extent of deep convection is preserved in gridded WSR-88D observations when there are overlapping observations from multiple radars. Gridded composites that overlap three or more radars yield a three-fold increase in the vertical resolution when compared to an individual radar (i.e., the usable Δz is reduced from $\sim$3 km on average to $<$1 km). The highest vertical resolution is attained when a single column or grid box has contributions from as many radars as possible.

Following this approach, Solomon et al. (2014) combine multiple radars in the NEXRAD network to study the occurrence of tropopause-penetrating convection at 3-hour intervals for 2004 over the eastern United States. Their study finds a distinct geographic pattern as well as a diurnal and annual cycle in the frequency of overshooting convective events. A majority of events occur over the high plains around 0000 UTC ($\sim$1800 LT) during the summer season. Events occur most frequently during the summer season, with May hav-

ing the highest number of individual overshooting storms. Occurrence maps in Solomon et al. (2014) show that overshooting events are infrequent east of the Mississippi River, which differs from the results of Bedka et al. (2010), who found overshooting frequently across the southeast United States. Because Solomon et al. (2014) analyzed one year of data with a 3-hour temporal resolution, the types of questions that can be addressed are limited. Most importantly, it is not clear whether 2004 was a typical year or whether there is significant variability from year to year. Bedka et al. (2010) presented a 5-year climatology of overshooting convection using satellite data, which raises the question of what is responsible for the difference. Is it due to differences in the retrieval methods or to interannual variations?

One important factor that can affect the amount of overshooting convection is the height of the tropopause, which varies with latitude and season. Studies of convection in the tropics have shown that storm tops are able to reach the cold point tropopause altitude but rarely exceed it (Alcala and Dessler, 2002; Gettelman et al., 2002; Dessler, 2002). Because the tropical tropopause is so high, storms are typically unable to penetrate into the lower stratosphere. In the extratropics, however, convective storms frequently penetrate through the tropopause into the lower stratosphere. Overshooting convection is uncommon in winter, though, despite lower tropopause heights, as shown by the annual cycle presented in Figure 8 of Solomon et al. (2014).

Another aspect of mid-latitude deep convection that has not been studied extensively is the extent of overshooting tops in terms of potential temperature, θ, which is a useful vertical coordinate in the stratosphere. Typically, potential temperatures at the extratropical and tropical tropopauses are $\sim$350 K and 380 K, respectively. Tropospheric air injected in the extratropical stratosphere to 380 K or above, sometimes referred to as the 'overworld', could potentially be transported isentropically to the tropical lower stratosphere where it can have an impact on the dynamics, chemistry, and radiation of that region as well.

In order to improve our understanding of overshooting convection, this research expands on the work done in Solomon et al. (2014) by analyzing 10 years of NEXRAD data at hourly intervals across the continental United States east of the Rocky Mountains. Because a large fraction of the deep convection occurs during the warm season, as shown by Solomon et al. (2014), we restrict the analysis to May, June, July, and August (MJJA). Increasing the sampling frequency and the length of the analysis period allows this study to address many of the questions raised by Solomon et al. (2014) using a much larger data set, and allows investigation of the interannual variability of overshooting convective events over a large region. Therefore, the goals of this research are to apply improved quality control procedures to the methods used in Solomon et al. (2014), to compare and expand upon their results with those from a much larger data set, as well as analyze the interannual variability of overshooting convection over a large part of the conterminous U.S.

2. DATA

2.1 NEXRAD Data

Radar data are obtained from the National Oceanic and Atmospheric Administration (NOAA) National Center for Environmental Information (NCEI) NEXRAD web service (http://www.ncdc.noaa.gov). NCEI was formerly known as the National Climate Data Center (NCDC). The NEXRAD Doppler S-band (10 cm) radars measure radar reflectivity factor Z_{H}, radial velocity V_{R}, and velocity spectrum width σ_{V} in a three-dimensional volume around the radar by scanning a conical beam with an angular width of 0.95° at multiple elevation angles (Crum and Alberty, 1993). The NEXRAD radars use two main volume-scanning strategies: 'clear-air mode' and 'convective mode'. The scan strategy affects the temporal resolution of each radar and depends upon conditions such as operating status and current weather conditions surrounding the radar. The radar operates in convective mode when convective events occur in the vicinity of the radar. When operating in convective mode, the radar completes a total volume scan in approximately 4.5-5 minutes (Crum and Alberty, 1993). Data files containing volume scans are classified as Level 2 data products.

Over the years, NOAA has modified the storage scheme for NEXRAD data to handle changes in data processing and radar capabilities. Level 2 data files created prior to May 2008 are referred to as 'legacy resolution'. Legacy-resolution files contain three primary variables, Z_{H}, V_{R}, and σ_{V}, stored with a resolution of 1° in azimuth and 1 km in range. Beginning in May 2008 NEXRAD products transitioned to 'super resolution', which has an azimuthal resolution of 0.5° and a range resolution of 250 m for the lowest 3-5 elevations (generally scans at 1.5° or lower). Beginning in May 2011, the NEXRAD radars were upgraded to have dual-polarization capabilities. The upgrade process was completed

throughout the NEXRAD network in 2013. Data files from the dual-polarization radars include additional variables, but they are not used in this study. Here we use only the horizontal reflectivity, Z_{H}.

NEXRAD radars are capable of sensing reflectivities well below those found in regions producing measurable precipitation, especially at ranges close to the radar. The minimum detectable signal of the radar is -42 dBZ at 1 km and increases with increasing range to about 11 dBZ at the maximum detectable range of 460 km (Crum and Alberty, 1993). At 300 km, which is the maximum range used in this study for compositing multiple radars, the minimum detectable signal is $\sim$7.5 dBZ (Homeyer, 2014).

Figure 2.1 (a) shows the study area and the best possible radar coverage, assuming that all radars are operating. To maximize the overlap between nearby radars and produce

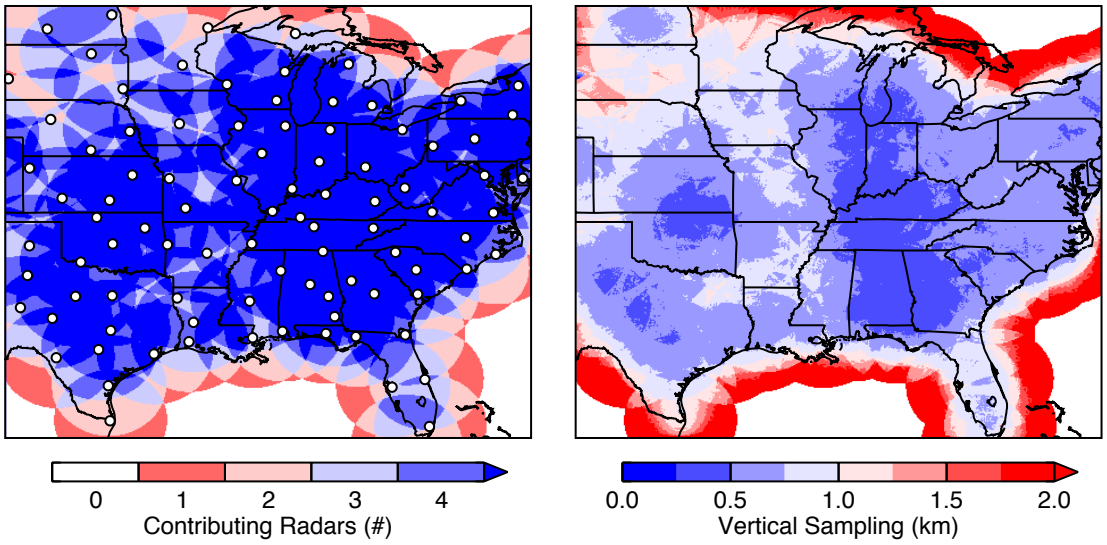

Figure 2.1: a) Left image shows the number of contributing radars to the composite for eastern portion of United States (300 km radial distance from radar). b) Vertical resolution attained from combining overlapping radars (Homeyer, 2016 personal communication).

the highest-quality gridded product, the domain is restricted to the U.S. east of the Rocky

Mountains, where radar coverage is densest (longitude bounds: 257.0°–285.0°, latitude bounds: 25.0°–48.0°). This region includes 104 of the network's 160 radar sites, which are listed in Table 2.1.

Table 2.1: NEXRAD radar stations data are collected for in the analysis.

KABR	KAKQ	KAMA	KAMX	KAPX	KARX	KBGM	KBIS
KBMX	KBRO	KBUF	KBYX	KCAE	KCCX	KCLE	KCLX
KCRP	KCXX	KCYS	KDDC	KDFX	KDGX	KDIX	KDLH
KDMX	KDOX	KDTX	KDVN	KDYX	KEAX	KENX	KEOX
KEVX	KEWX	KFCX	KFDR	KFDX	KFFC	KFSD	KFTG
KFWS	KGLD	KGRB	KGRK	KGRR	KGSP	KGWX	KHGX
KHPX	KHTX	KICT	KILN	KILX	KIND	KINX	KIWX
KJAX	KJGX	KJKL	KLBB	KLCH	KLIX	KLNX	KLOT
KLSX	KLTX	KLVX	KLWX	KLZK	KMAF	KMBX	KMHX
KMKX	KMLB	KMOB	KMPX	KMQT	KMRX	KMVX	KMXX
KNQA	KOAX	KOHX	KOKX	KPAH	KPBZ	KPOE	KPUX
KRAX	KRLX	KSGF	KSHV	KSJT	KSRX	KTBW	KTLH
KTLX	KTWX	KTYX	KUDX	KUEX	KVAX	KVNX	KVWX

Some of the stations listed are just outside the bounds of the domain but are included because they are able to contribute their beams to grid boxes within the domain area. Figure 2.1b shows the nominal vertical resolution obtained at each location, again assuming that all radars are operating.

For various reasons, data are not always available for every radar. The actual fraction of time covered by three or more radars during the study period is shown in Figure 2.2 which draws a theoretical 300 km radius circle around the radar site. The domain, eastern United States, is chosen due to its high radar density, but radar coverage is not perfect. There are a few areas on the map that are unable to achieve the 3+ radar contribution criteria so the measurements do not have sufficient weight in order to be gridded. Thus,

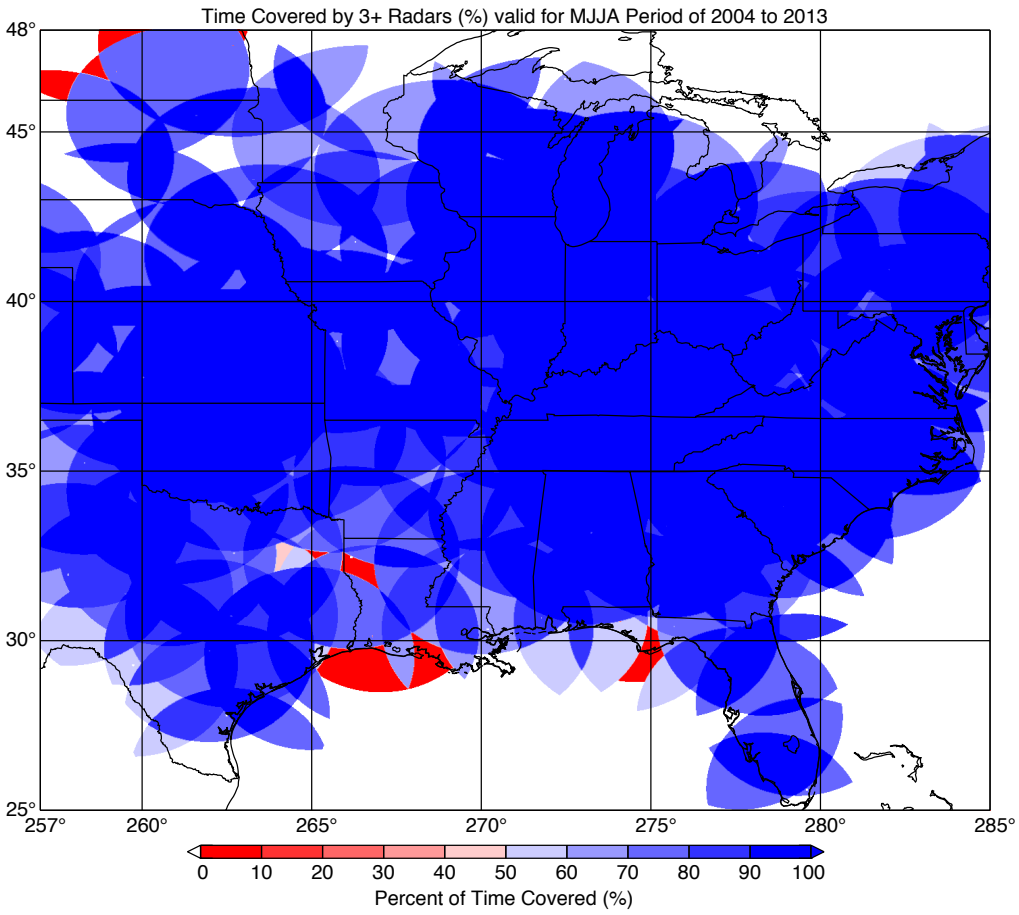

Figure 2.2: Fraction of time each grid point in the study domain is covered by three or more radars.

we end up with some missing information. Radar stations also periodically go offline for extended periods of time for various reasons. This creates locations on the map that have a very low fraction of 3+ radar coverage (light blue and red shading).

2.2 ERA-Interim Reanalysis

To identify tropopause-penetrating convection, instantaneous tropopause heights are calculated using ERA-Interim (ERA-I) reanalysis data, supplied by the European Centre for Medium-Range Weather Forecasts (EMCWF) (Dee et al., 2011). The ERA-I data cover the period from 1979 to the present and are obtained from the National Center for

Atmospheric Research archive (http://rda.ucar.edu/datasets/ds627.0/). The ERA-Interim reanalysis is produced with a sequential data assimilation scheme, advancing forward in time using 12-hourly analysis cycles to grid estimates of three-dimensional (3-D) meteorological variables (Dee et al., 2011). Data are provided at 6-hourly synoptic times (00, 06, 12, and 18 UTC) with a horizontal resolution of $\sim$0.7° x $\sim$0.7° on a global Gaussian grid and 37 irregularly-spaced pressure levels extending from 1000 to 1 hPa. Because the data are not on the same grid as the NEXRAD data, temperature T and geopotential height Z are linearly interpolated in space and time onto the NEXRAD grid. The tropopause height, z_T, is then calculated on the NEXRAD grid by applying the World Meteorological Organization (WMO) definition (WMO, 1957) of the tropopause to each atmospheric column.

ERA-Interim data are also used in this study to calculate the potential temperature at the echo-top height. Using the temperature, T, values in the reanalysis the potential temperature at each pressure level is calculated by applying Equation 2.1.

$$\theta = T(\frac{p_0}{p})^{\frac{R}{c_p}} \tag{2.1}$$

In this equation, θ represents the potential temperature, p_0 is the standard pressure (1000 hPa), p is the pressure, and R/c_p is the ratio of the gas constant to the specific heat capacity of air at constant pressure. The value used for R/c_p is 2/7 because air is primarily composed of diatomic gases. Once the potential temperature is calculated at the ERA-I pressure levels, we compute the potential temperature at discretized heights using the geopotential height and linearly interpolate to the height of the echo-top.

2.3 Radiosonde Data

Due to their high vertical resolution, radiosonde data are used in this study to assess the quality of tropopause height calculations from the ERA-I reanalysis. The instruments used

in this study take measurements approximately every 30 m during ascent. The radiosondes are operated by the National Weather Service. Figure 2.3 shows a map of the stations in the United States where the radiosondes are released.

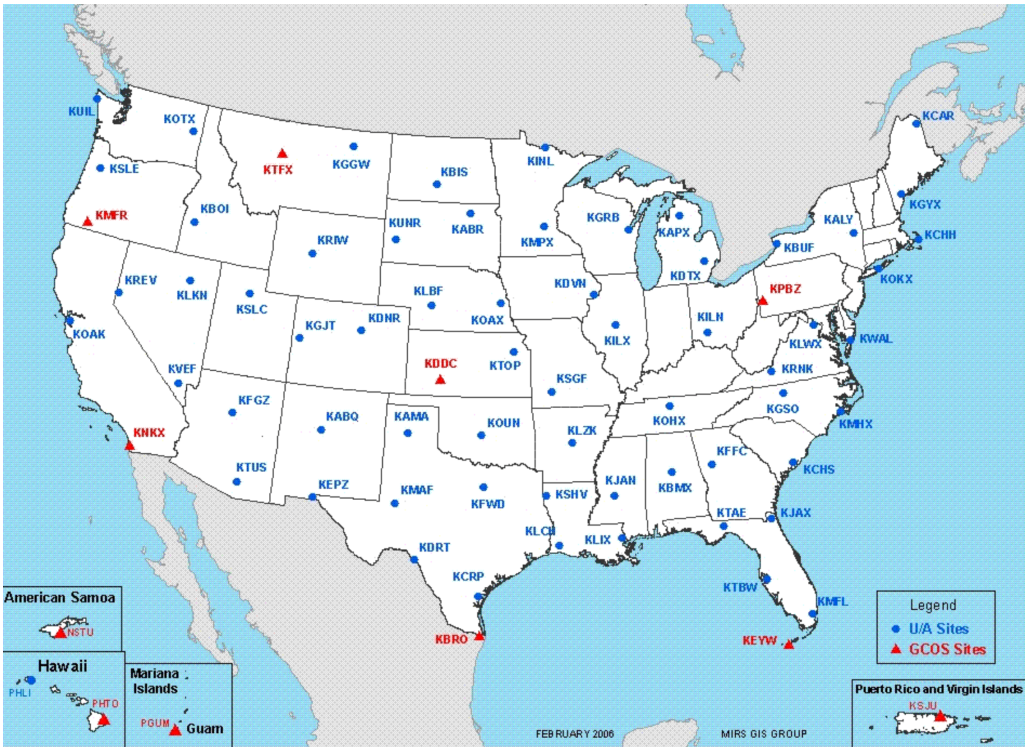

Figure 2.3: Stations in the United States that collect radiosonde measurements (NWS, 2016).

Radiosonde data from the stations within our study domain are downloaded from the archive at the NOAA Earth System Research Laboratory (http://www.esrl.noaa.gov/raobs/).

3. METHODS

3.1 Downloading and Ordering NEXRAD Data

Before downloading NEXRAD Level 2 data from NCEI via ftp, files must first be ordered and staged from tape to disk. The downloaded files are tar archives containing compressed volume scan files. Orders are placed interactively via the NCEI website. This study uses data from 104 radar stations for the MJJA period 2004 to 2013. Due to the large volume of data, the bulk ordering method is used. Bulk orders are limited to 250 GB per order. For legacy resolution data that translates to one year of data for three or four stations. For super-resolution and dual-polarization data, bulk orders typically can contain only one or two stations per year. The entire process of ordering and downloading one bulk order typically takes three days. Due to bandwidth limitations at NCEI and issues with the website, downloading the entire 10-year archive took approximately eighteen months. Table 3.1 shows the amount of space required to store the MJJA season for each year of the climatology. Due to the changing number of available stations and the increasing file sizes over time, the storage volume ranges from $\sim$2.2 TB for 2004 to $\sim$13.9 TB for 2013.

Under a contract between NOAA and Amazon, the NEXRAD data archive is now available via Amazon Web Services (AWS), which allows much faster access to NEXRAD data and eliminates dealing with tar files.

3.2 NEXRAD Compositing

Data from multiple NEXRAD radars are merged into a hourly, high-resolution, three-dimensional, gridded synoptic analyses using the methods described in Homeyer (2014) and Homeyer and Kumjian (2014). The analysis grid has grid boxes with a horizontal spatial resolution of 0.02° ($\sim$2 km) in longitude and latitude and a vertical resolution of 1 km. See Homeyer (2014) and Figure 2.1 (b) above for more details on the resolution achieved

Table 3.1: Space required to store compressed Level 2 NEXRAD data for each year's MJJA season.

Year	Storage Space (TB)
2004	2.2
2005	2.4
2006	2.3
2007	2.4
2008	3.7
2009	5.4
2010	5.8
2011	6.0
2012	8.9
2013	13.9
Total	53.1

in NEXRAD radar compositing. In this study, the data are processed at hourly analysis times (00, 01, ..., 23 UTC) using all available volume scans within a $\pm$10 minute window centered on the analysis time. The volume scan times correspond to the start time of that volume scan. The time at each elevation scan is estimated using the start time and duration to complete a scan. Since radar volume scans are irregularly taken approximately every 4.5 minutes in operating convective mode, the time window allows for scans taken just off of the hour to be linearly interpolated to the hourly analysis times. Figure 3.2, which is discussed further below, is an example of the composited radar reflectivity product.

The primary radar variable of interest in this study is the instantaneous, two-dimensional, gridded echo-top height, which is computed for each hourly, three-dimensional reflectivity field. Before computing the echo-top heights, however, the reflectivity fields are subjected to three quality control processes. First, 'echo holes' in the NEXRAD composites are found and filled. An echo hole is a gap in a reflectivity profile that is no more than a single level deep with valid measurements in the altitude bins immediately above and below

that level. Echo holes are filled by averaging the reflectivity and weighted reflectivity of the two surrounding altitude bins (Homeyer and Kumjian, 2014). Second, the NEXRAD data is decluttered following the approach outlined in Zhang et al. (2004). This is done in order to remove the various types of clutter that can arise in the 3-D regional NEXRAD composites. Following decluttering, the NEXRAD data are filtered by finding data points with low weights and removing them from the analysis. The resulting fields are used for the echo-top height analysis.

3.3 Echo-Top Height Identification

The echo-top height, z_e, is defined as the highest altitude in each column with a reflectivity that exceeds a specified threshold, with additional conditions discussed below. Echo-top heights are discretized into 1 km levels as a result of the vertical resolution attained in the NEXRAD data compositing. Due to the limited sensitivity of the radars to small particles, the identified echo-top height is not, in general, the cloud top height. The nominal reflectivity threshold for the existence of a valid echo is $\sim$7.5 dBZ (Homeyer, 2014). A lower reflectivity threshold might potentially provide a better estimate of the cloud-top height, but would also result in a higher incidence of errors and artifacts due to ground clutter and side-lobe contamination. After extensive testing with different thresholds, we conclude that a threshold of 10 dBZ provides the best balance between sensitivity and noise.

The echo-top altitude for each column is nominally the highest level with a reflectivity greater than or equal to 10 dBZ. To reduce the number of false echo-top identifications in situations with unrealistic reflectivity profiles, we require that the two altitude levels immediately below a potential echo-top also contain valid reflectivity measurements. If this condition is not met, the column is searched for the next highest echo exceeding 10 dBZ and the process is repeated until a valid echo-top is found or the bottom of the column

is reached.

The echo-top height relative to the tropopause, $z_r = z_e - z_T$, is computed from the NEXRAD echo-top height fields and the simultaneous ERA-Interim-derived tropopause height fields. To provide a more physical framework for the following analysis, contiguous regions of overshooting columns (grid boxes) are grouped into what we refer to as 'storms'. Grid boxes are defined as contiguous if they are adjacent at the sides or corners. Figure 3.1 presents an example of how the storms are defined by grouping adjacent grid boxes.

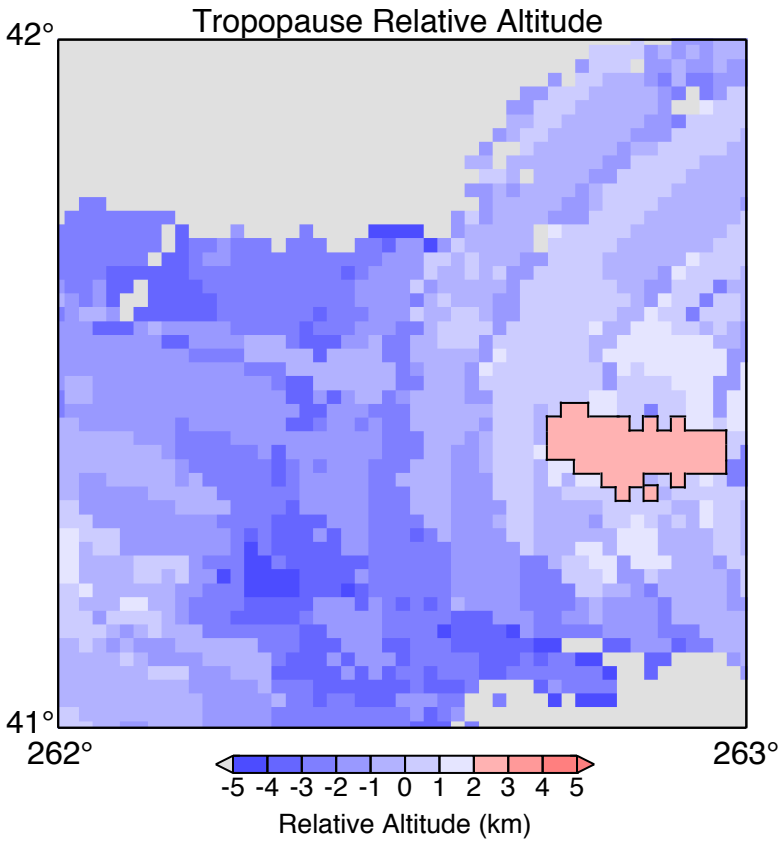

Figure 3.1: This image shows one +2 km identified storm on May 9, 2004 at 01Z. The +2 km storm is shaded in light red and outlined in black. The isolated grid box, adjacent to the to the rest of the storm, is considered part of that storm. Each column (grid box) within the +2 km storm has a tropopause-relative altitude $\geq$ 2 km.

To minimize uncertainties from the tropopause and echo-top calculations, and to focus on deeper storms that are likely to have more impact on the stratosphere, in this study, we analyze only those storm events that have $z_r \geq 2$ km. This paper will refer to these as +2 km storms. For a contiguous grid box to be grouped into one of these storms, the column must overshoot the tropopause by 2 km or greater. The number of distinct storms, using the same criteria above, at tropopause-relative altitude levels +0 km, +1 km, +2 km, +3 km, and +4 km is displayed in Table 3.2.

Table 3.2: Number of storms at or above set altitude levels above the tropopause.

Tropopause-Relative Altitude (km)	Number of Storms
+0	633,255
+1	174,075
+2	38,292
+3	7,191
+4	1,124

During the study period there are 38,292 distinct +2 km storms. The remainder of this paper focuses only on analysis and data quality control conducted using these +2 km storms.

3.4 Quality Control

After calculating all of the 10 dBZ echo-top heights for the MJJA period of 2004-2013 and grouping the overshooting grid boxes into storms, a sample of the +2 km storms is evaluated to confirm the echo-top identification. Storms are evaluated by visually inspecting composite reflectivity maps, tropopause-relative altitude maps, and vertical reflectivity cross-sections through the center of each sampled storm. Each inspected storm is sub-

jectively assigned to one of three categories: valid, invalid, or uncertain. Storms deemed invalid or uncertain are removed from further analysis. Figure 3.2 provides an example of a valid overshooting storm. The classification is based on the strong and continuous vertical reflectivity structure and the realistic reflectivity map. Examples of storms deemed uncertain and invalid are presented in Figures 3.3 and 3.4, respectively.

To create a targeted sampling scheme for the storms, the population is partitioned into 5 overlapping groups based on the maximum reflectivity that occurs in the storm and z_e or z_r. The partitioning is demonstrated in Figure 3.5. The five groups are:

1a: Deep storms with $z_e \geq 20$ km (light gray region in Figure 3.5 (a))

1b: Deep storms with $z_r \geq 5$ km (light gray region in Figure 3.5 (c))

2a: Storms with relatively high z_e and low reflectivity (dark gray region in Figure 3.5 (a))

2b: Storms with relatively high z_r and low reflectivity (dark gray region in Figure 3.5 (c))

3: Storms that are not in groups 2a or b (unshaded region in Figure 3.5 (c))

This study does not inspect 36,890 of the 38,292 identified storms. Every storm in groups 1a, 1b, 2a, and 2b are inspected. A sample of 1000 storms from group 3 is also analyzed. The results of the visual inspection are provided in Table 3.3. Note that because two different altitude criteria are used, there is overlap between some of the groups. Group 3, however, does not have any storm overlap with the other groups.

Table 3.3 shows the number of storms in each group and the corresponding percentages of storms classified as valid, invalid, and uncertain in that group. The majority ($\sim$63% and $\sim$76% for $z_e \geq 20$ km and $z_r \geq 5$ km, respectively) of deep storms are valid. In group 1a, the valid storms are primarily those with z_e of 20 or 21 km and maximum storm reflectivities $>$40 dBZ. In group 1b, the valid storms are primarily those with z_r between

5 and 7 km and maximum storm reflectivities >50 dBZ. In both groups a few very deep storms have realistic reflectivity profiles. About half the storms in groups 2a and b are found to be valid. A large fraction of the inspected storms in group 3 are valid, with less than 0.5% identified as invalid or uncertain.

Figures 3.5 (b) and (d) show the number of storms, the number of storms inspected, and status of the inspected storms at each altitude level in terms of z_e and z_r. Note that the abscissas in these plots are logarithmic. In general, the fraction of invalid or uncertain storms increases with height above the tropopause.

Figure 3.6 provides a map of the +2 km storms and their respective status plotted at the maximum echo-top height location in the storm. There appears to be no distinct pattern of the location of overshooting storms identified as invalid or uncertain, which indicates that there are no systematic geographic factors causing the misidentifications. All of the storms classified as uncertain and invalid are removed for the following statistical analysis. After eliminating these cases, there are 38,158 +2 km storms remaining for analysis. Based on the number of invalid and uncertain storms identified in the sample from group 3, we estimate that approximately 150 ($< 0.4\%$) of the storms in analysis population are invalid and uncertain. Because of the exhaustive analysis of groups 1 and 2, we believe that all of the very high storms in the analysis population are valid.

Table 3.3: Status of +2 km storms reviewed for each group.

Status	Group 1a	Group 1b	Group 2a	Group 2b	Group 3
number of storms	112	160	142	87	1000
valid	60.7%	75.0%	55.6%	35.6%	99.6%
invalid	33.9%	20.6%	34.5%	55.2%	0.1%
uncertain	5.4%	4.4%	9.9%	9.2%	0.3%

3.5 Comparing ERA-I and Radiosonde Calculated Tropopauses

The accuracy of calculations from data derived through observations in reanalyses is open to some debate. Deep convective events have the ability to perturb the tropopause height (Homeyer and Kumjian, 2014). How the tropopause is perturbed by these events, as well as to what degree these perturbations are captured by the ERA-I data, is not yet known. This makes quantifying the uncertainty in these calculations difficult to asses. By observing deeper storms that protrude at least 2 kilometers into the stratosphere, we are able to eliminate much of the uncertainty in quantifying overshooting events. This, however, is not sufficient to disregard the uncertainty in the tropopause calculations.

To test the quality of the tropopause height calculations from the ERA-I dataset, we compare the heights with those calculated from high vertical resolution radiosonde data. In order to validate the ERA-I tropopause calculations, the methods follow those outlined in Solomon et al. (2014) where the calculations are investigated by plotting the difference between the ERA-I tropopause and radiosonde tropopause. The results of this study, provided in their Figure 2 for the year 2004, show that the two datasets agree well, with 91% of the ERA-I tropopause heights within ± 1 km of the radiosonde calculated heights. Figure 3.7 uses the MJJA season of 2010 as an example to show the difference in tropopause heights calculated from the two datasets.

The tropopause heights calculated from ERA-I, for each MJJA season of our climatology, consistently have over 88% of values within 1 km of the radiosonde tropopause calculation. Most of the ERA-I heights also overestimate the tropopause height ($\sim$76%) when compared to the radiosonde calculations. This implies that any deep convective echo-top heights calculated to be 2 km or more above ERA-I tropopause heights are most likely, in fact, stretching into the lower stratosphere.

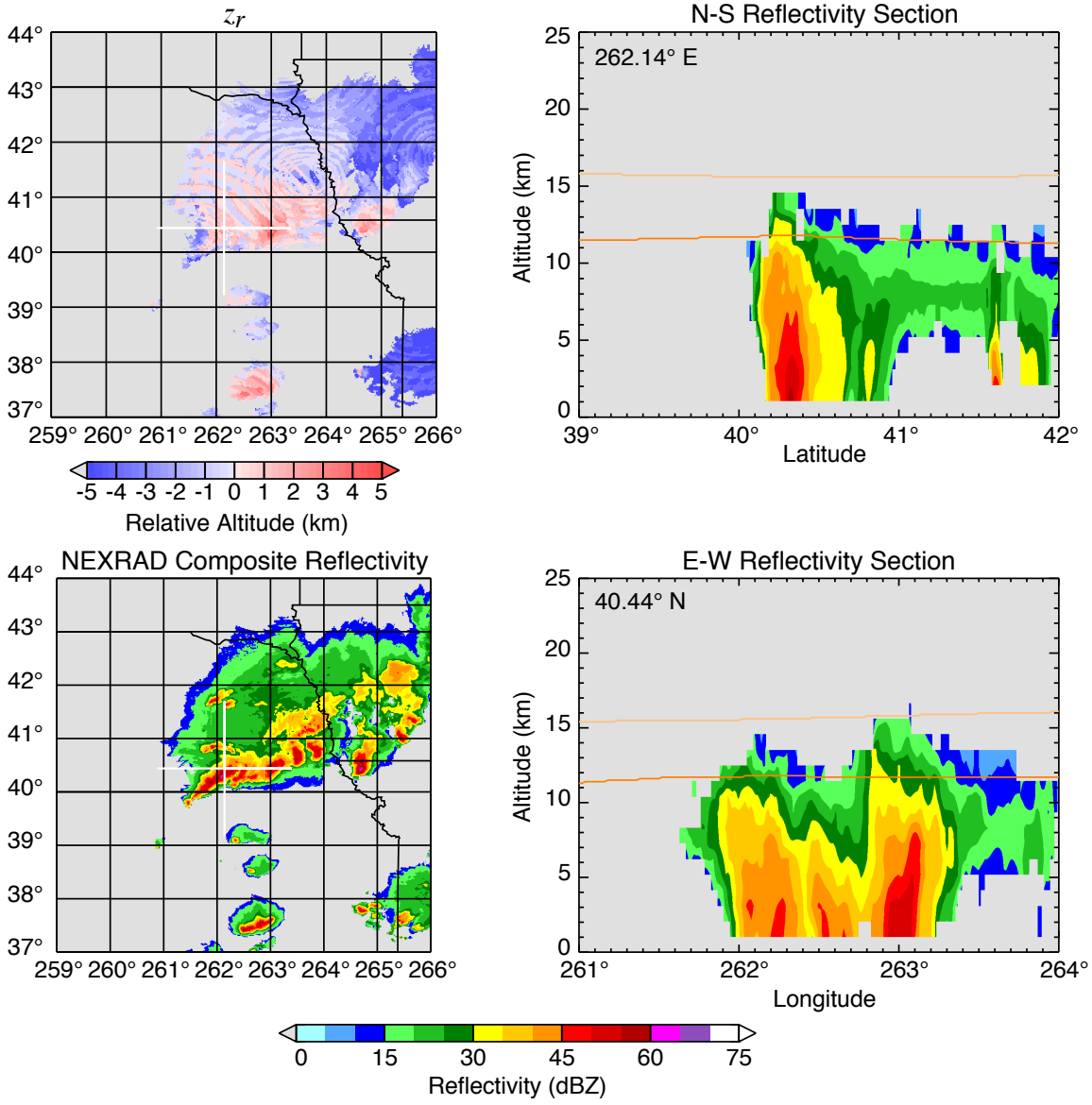

Figure 3.2: Four-panel image evaluated to confirm echo-top height identification of +2 km storm on June 12, 2004 at 2300Z. The dark orange line across the vertical cross-section plots, latitude-altitude and longitude-altitude indicates the height of the primary tropopause. The lighter orange line indicates the secondary tropopause. Note that every four-panel image did not have both the primary and secondary tropopause identified. The crosshair drawn in white on the reflectivity and tropopause-relative maps is centered over the center of the storm.

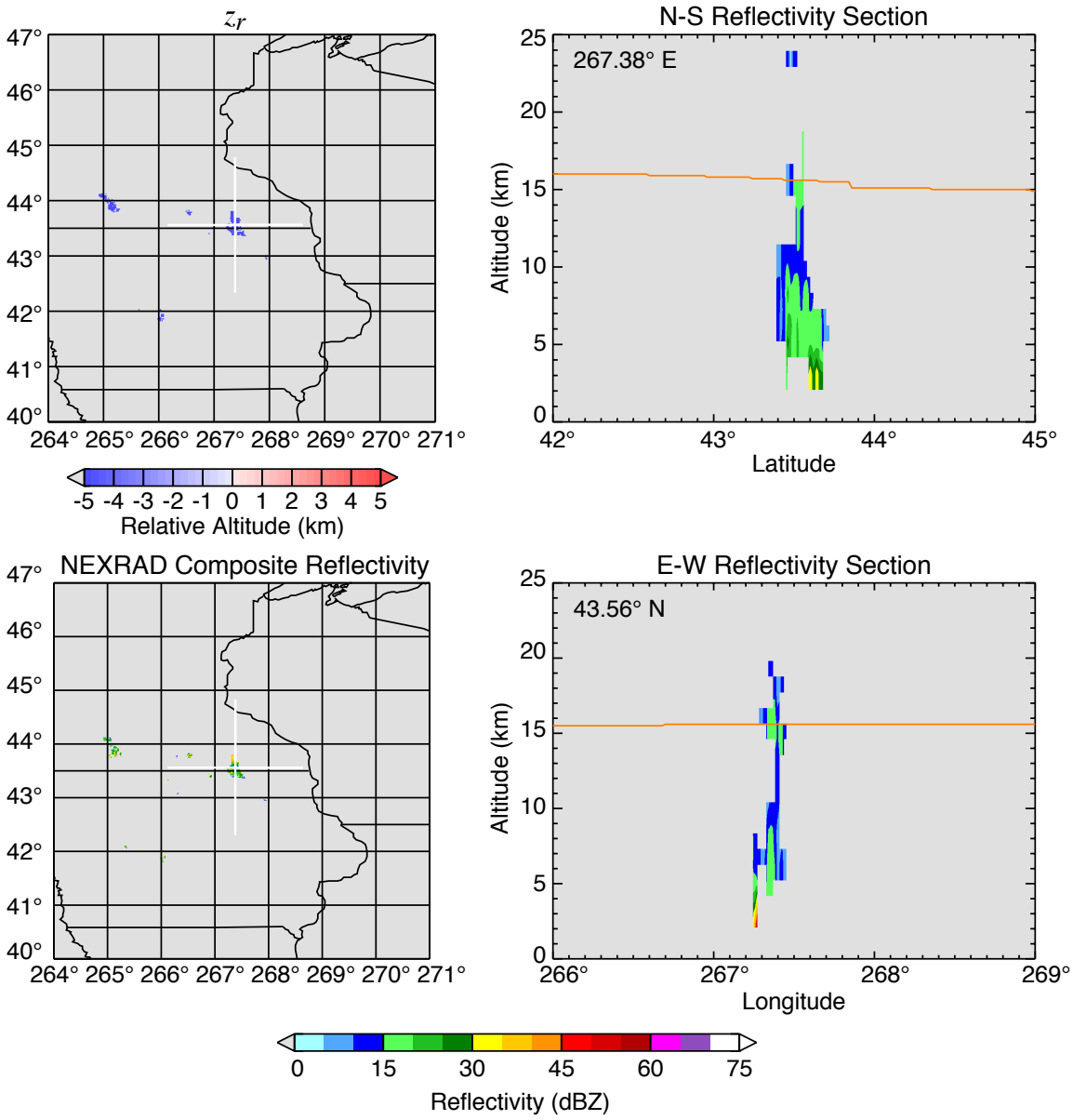

Figure 3.3: Four-panel image evaluated to confirm echo-top height identification of +2 km storm on July 25, 2011 at 1400Z. There is not enough information in this image to definitively say whether or not the radar return is valid. Thus, it is deemed uncertain and the storm is removed from further analysis. The crosshair drawn in white on the reflectivity and tropopause-relative maps is centered over the center of the storm.

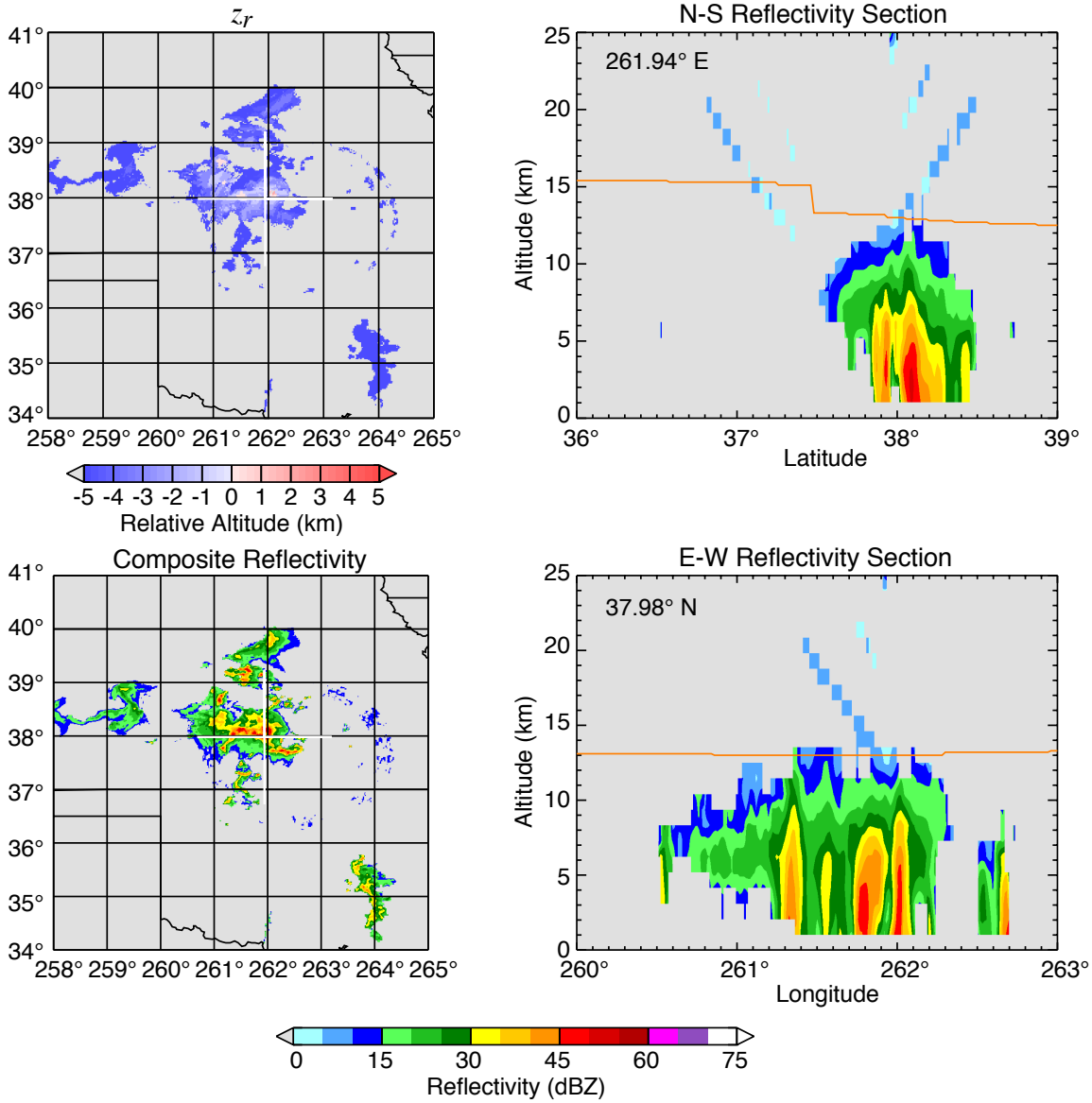

Figure 3.4: Four-panel image evaluated to confirm echo-top height identification of +2 km storm on August 16, 2004 at 1100Z. This reflectivity return clearly has contribution from bad data measurements. The diagonal lines in the vertical cross-section plot above the tropopause, in orange, appears to be a result of side-lobe contamination. This storm is deemed invalid and removed from further analysis. The crosshair drawn in white on the reflectivity and tropopause-relative maps is centered over the center of the storm.

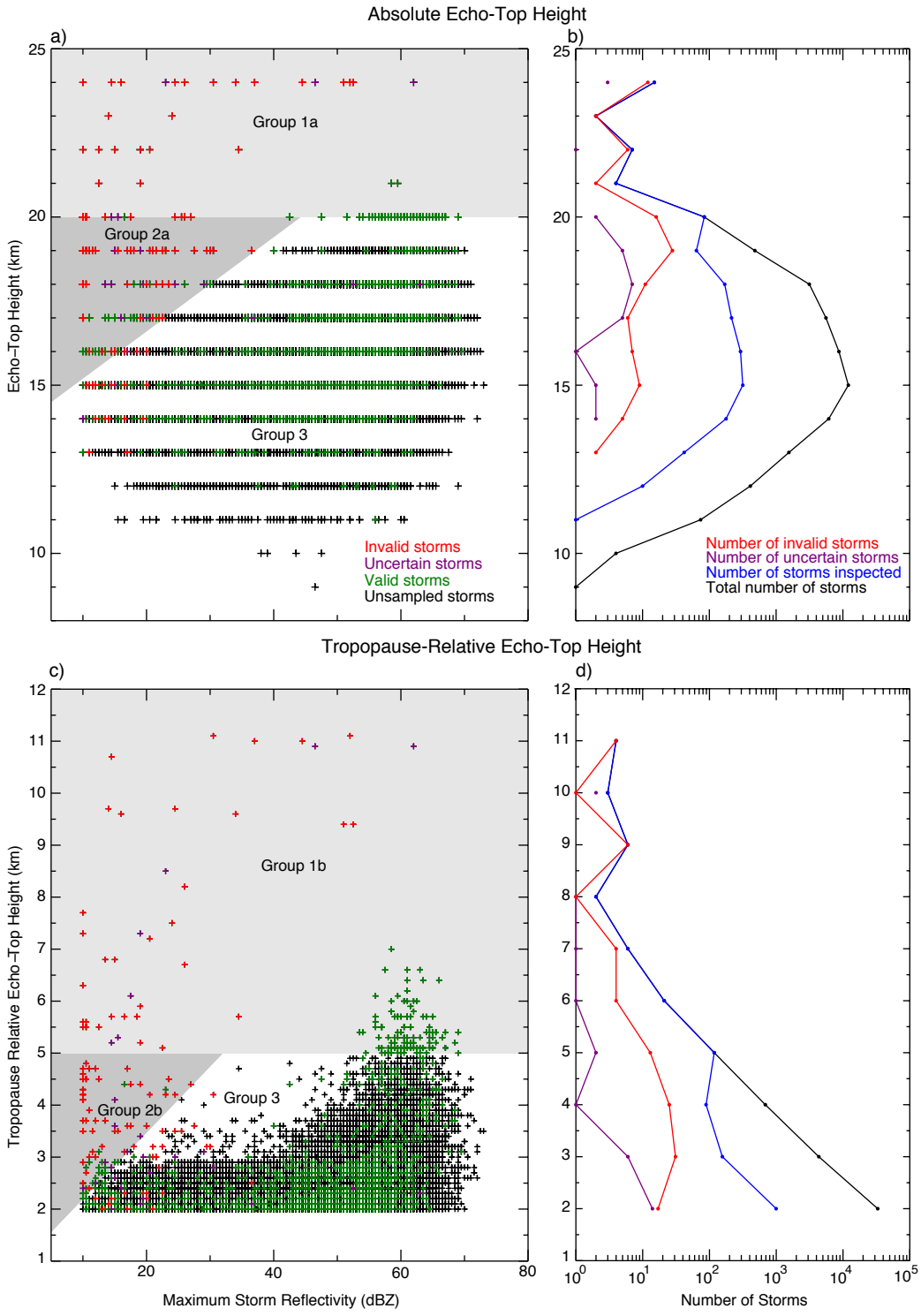

Figure 3.5: a) Scatterplot of maximum echo-top height z_e in each storm as a function of maximum reflectivity in the storm. b) Number of echo-tops as a function of altitude (black); number of storms inspected at each level (blue); number of invalid and uncertain storms at each level (red and purple, respectively. c) Same as (a) but for z_r. d) Same as (b) but for z_r.

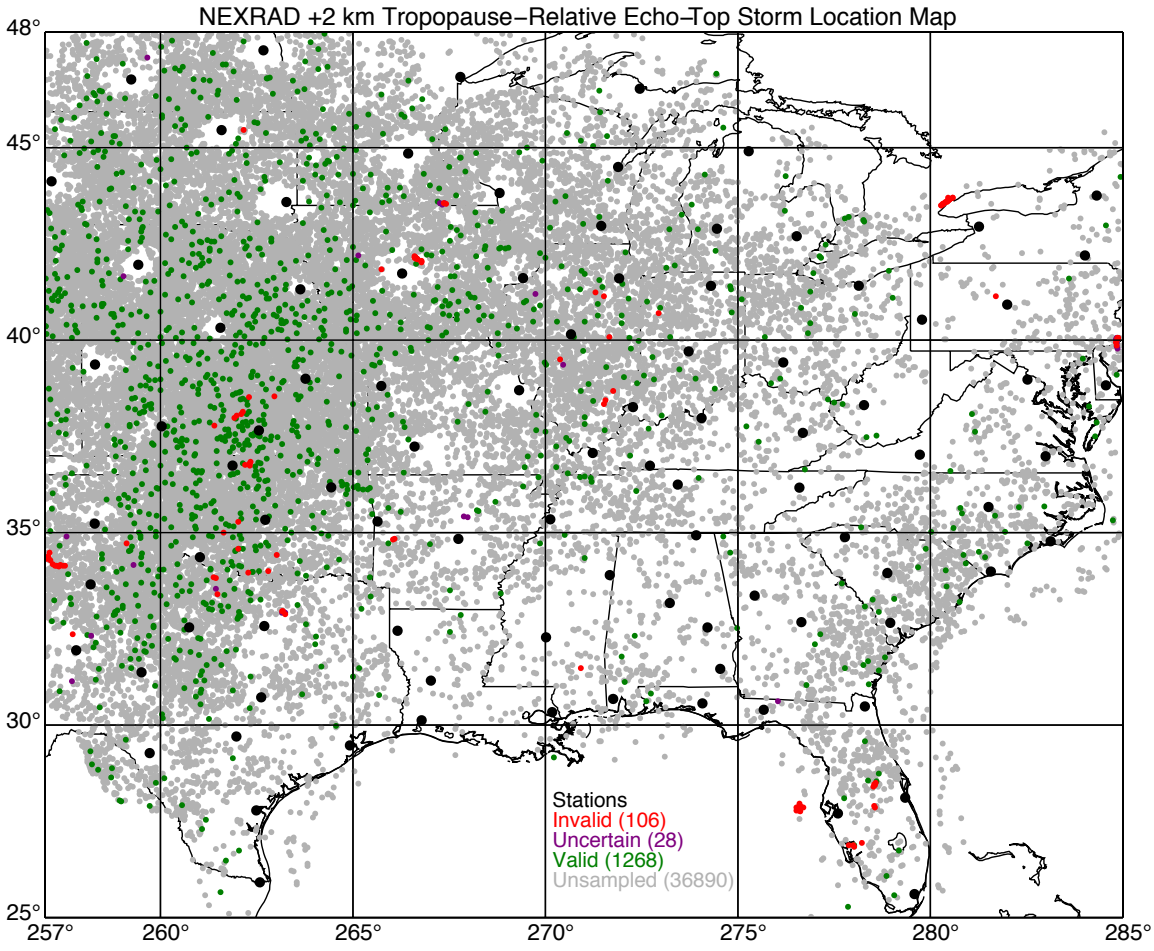

Figure 3.6: Map of the maximum echo-top heights within each +2 km storm and the storm's respective status. This map plots in order: unsampled, valid, uncertain, and invalid storms.

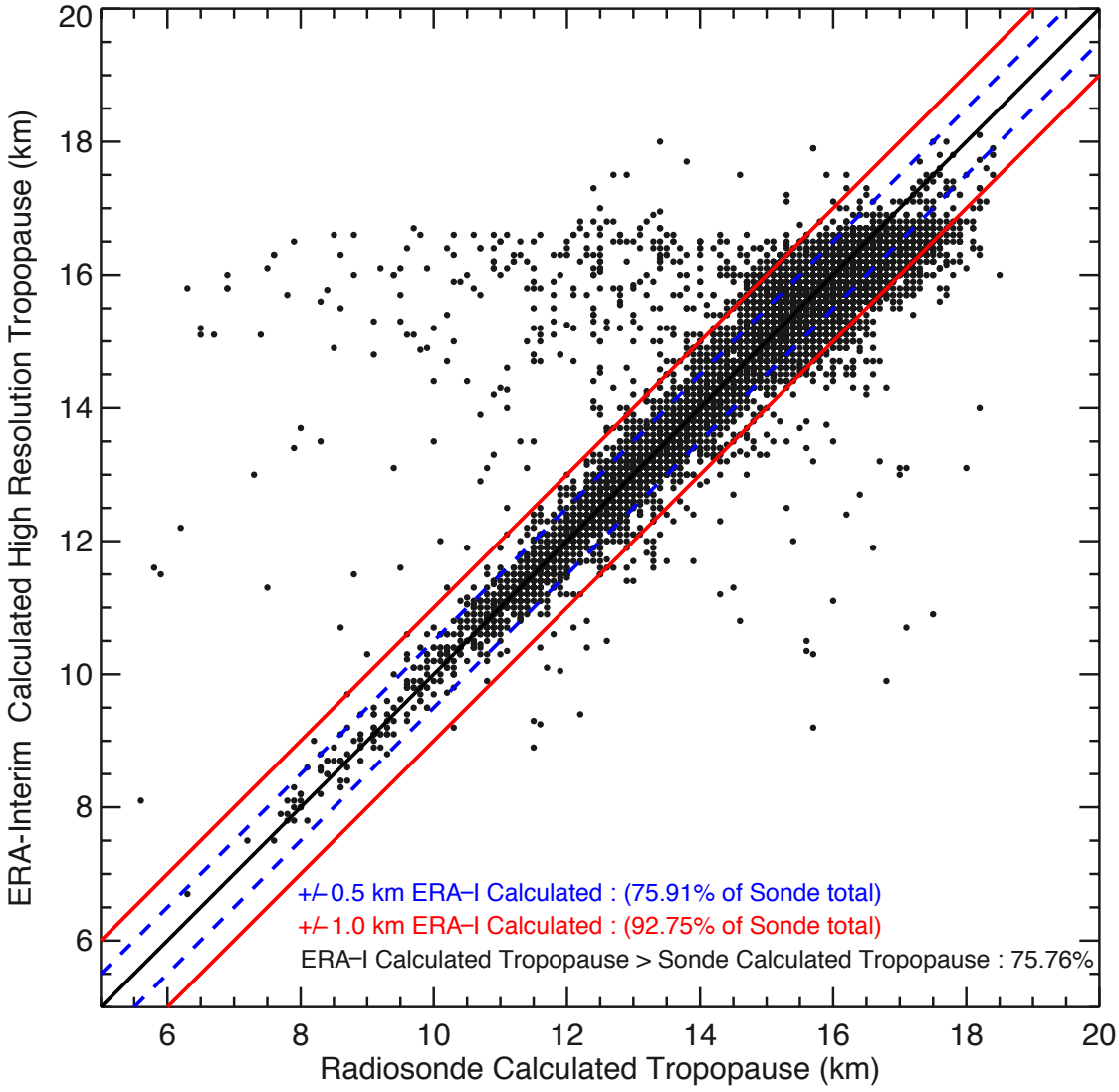

Figure 3.7: Comparison of tropopause altitudes computed from radiosondes and from the ERA-Interim reanalysis (Solomon et al., 2014). Points between the red lines are values that agree within ± 1 km. Points between the dashed blue lines are values that agree within ± 0.5 km.

4. RESULTS

4.1 Overview

Here we present an analysis of overshooting storms that extend at least 2 km above the ERA-I calculated primary tropopause. It is important to note that the following results exclude a large number of shallow overshooting storms that penetrate less than 2 km into the stratosphere. Also, because individual overshooting events can last as little as 5 or 15 minutes with the standard Brunt-Vaisala period in the lower stratosphere approximately 5 minutes, some overshooting storms are missed by the hourly analysis. Therefore, the total number of actual overshooting events is higher than the numbers presented here. That question will be addressed in future research using reflectivity analyses with better temporal resolution.

Each May through August season contains 123 days, so this 10-year study comprises a total of $24 \times 123 \times 10 = 29{,}520$ instantaneous hourly analyses. The total area of the study domain is 6.37×10^6 km^2. A total of 38,158 storms are included in the following analysis. On average this corresponds to approximately 3,815 storms per year or 31 storms per day. As discussed in Section 3.4, approximately 0.4% of these storms may be incorrectly identified due to errors in the reflectivity data, but the impact on the statistics should be minimal. The overshoot region of the storms range in size from 1 to 1,713 grid boxes. Figure 4.1 is a histogram of the size of the overshooting tops. The median number of grid boxes in a storm is 3. The histogram appears to have two distinct regions following power law behaviors. The first region, number of grid boxes ≤ 20, falls off by a power of approximately -4/3. The second region, number of grid boxes ≥ 50, decreases by a power equal to about -2.

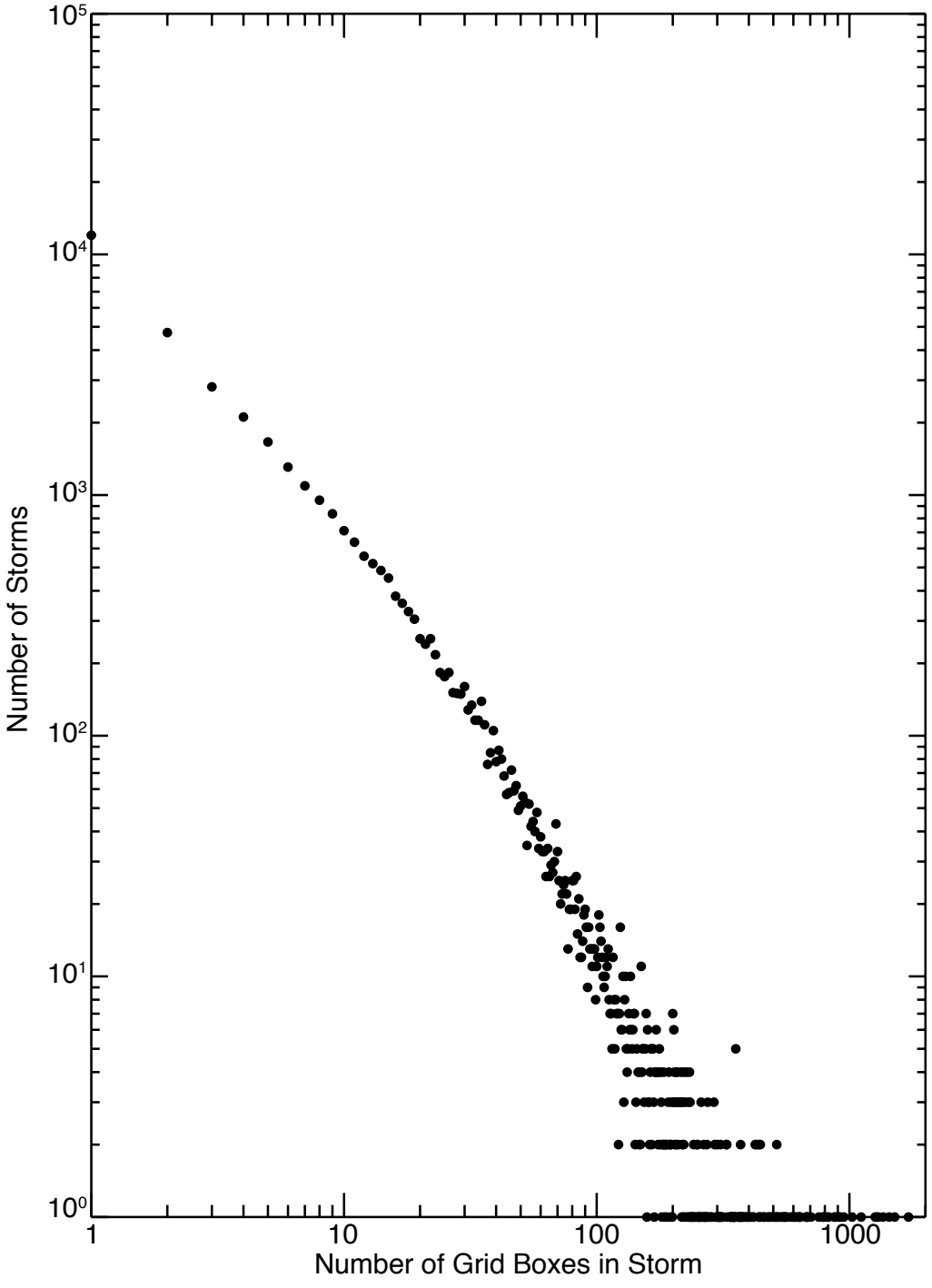

Figure 4.1: Histogram of the storm size in grid boxes. The bin size is 1.

4.2 Monthly and Interannual Variations

The number of years added to this study, compared to others, makes it possible to analyze monthly and interannual variations of overshooting storm events. Figure 4.2 shows the number of storms during each month for the entire study period. May and June typically have more storms than July and August, with May containing on average approximately three times as many storms as August. The largest number of overshooting events for any month is observed in May 2013. The color scheme in Figure 4.2 is used throughout the paper for all figures that show annual values.

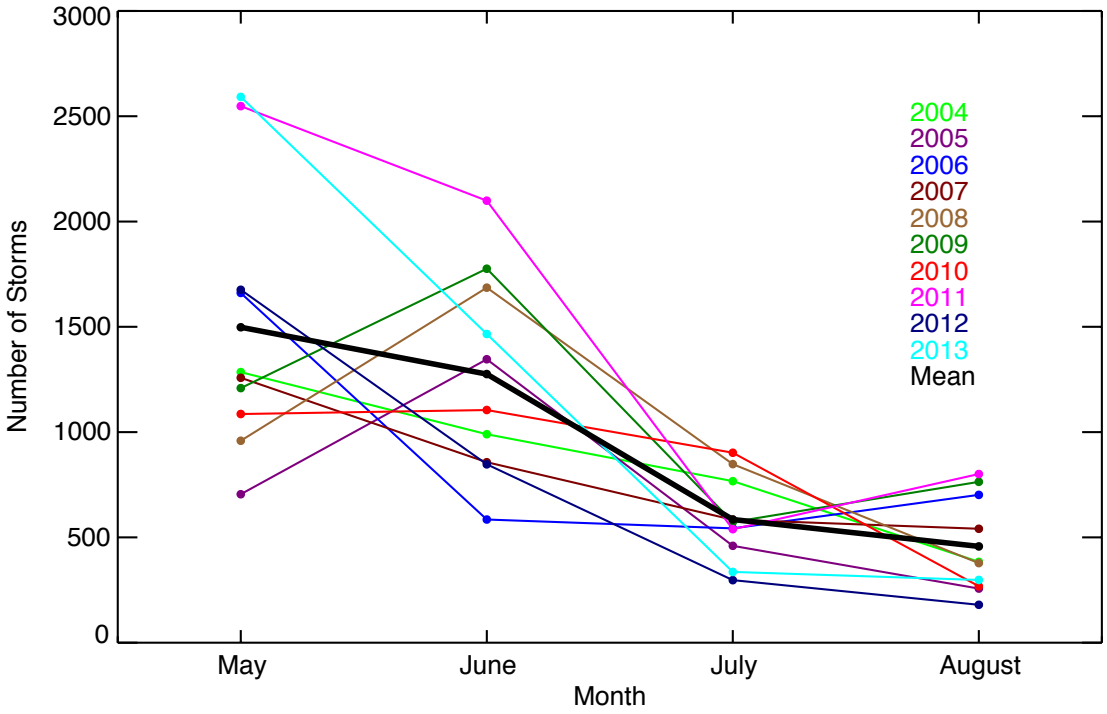

Figure 4.2: Number of +2 km storms per month for each year. Each color on the plot corresponds to a given year shown in the key. The bold black line shows the average for each month.

Figure 4.3 shows the total number of +2 km storms for each year (top panel) and the total overshooting volume for those years (bottom panel). Overshoot volume is computed by using the calculated tropopause-relative height of each column within the +2 km storm and multiplying it by the associated grid box area. The number of overshooting storms varies by about a factor of two during the study period, with a minimum of 2,768 storms in 2005 and a maximum of 5,987 in 2011. The storm volume for each year follows a similar pattern to the occurrences. The minimum and maximum overshoot volumes are 3.5×10^5 km^3 in 2005 and 7.3×10^5 km^3 in 2011.

Figure 4.4 presents the interannual variations of the diurnal cycle of overshooting area and occurrences. There is a large diurnal cycle with a peak that consistently occurs from 22 to 02 UTC (late afternoon to early evening local time). The minimum number of events occurs between 14 and 18 UTC (late morning to early afternoon local time). The diurnal cycle of overshooting convection is consistent with the known diurnal cycle of summertime precipitation. Dai et al. (1999) analyzes diurnal cycle precipitation patterns using observations and models over the contiguous U.S. In their study, they discover a very strong late afternoon maxima of precipitation during the summer.

Storm overshooting area, in the bottom panel of the figure, is calculated by computing the overshooting area of each storm and then summing the areas for each year and analysis time. As was the case for the overshooting volume and number of storms per year, the diurnal cycle of storm area is very similar to the diurnal cycle of the number of storms. The greatest +2 km overshooting areas are observed between 22 and 02 UTC. The total overshooting area of the storms during the climatology is calculated to be 1.98×10^6 km^2.

Figure 4.5 illustrates the variation of the diurnal cycle by month. The variations in the diurnal cycle for the different months follow the changes in the total number of storms per month seen in Figure 4.2. The bottom panel of Figure 4.5 demonstrates that although the amplitude of the diurnal cycle varies by about a factor of four between May and August,

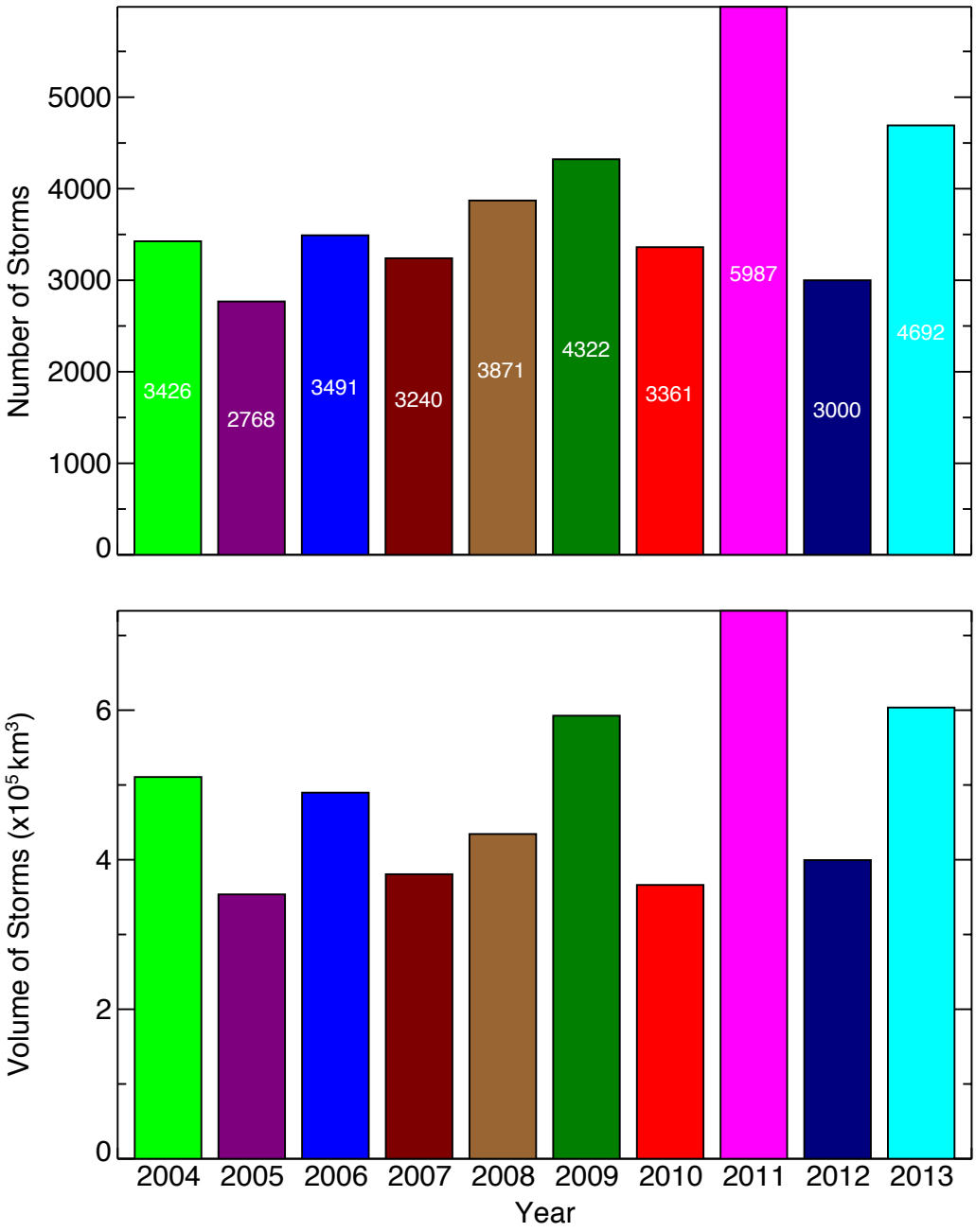

Figure 4.3: Top) number of +2 km storms during the MJJA season of each year. The numbers within the bars are the exact number of overshooting storms for that year. Bottom) total storm overshooting volume for each MJJA season.

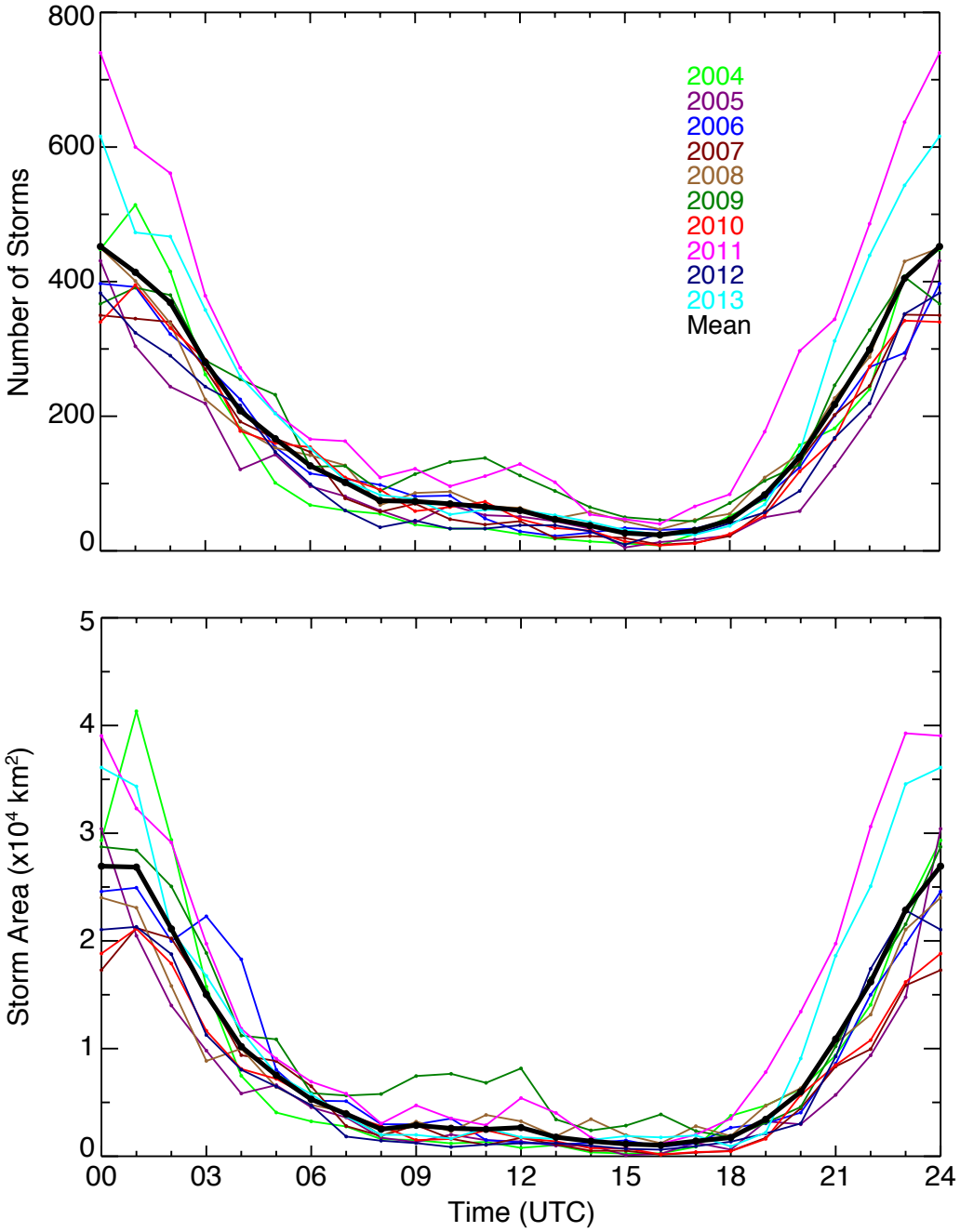

Figure 4.4: Top) diurnal cycle of the number of overshooting storms for each year. Bottom) diurnal cycle of storm area for each year. The bold black line is the climatological mean for the 10-year period.

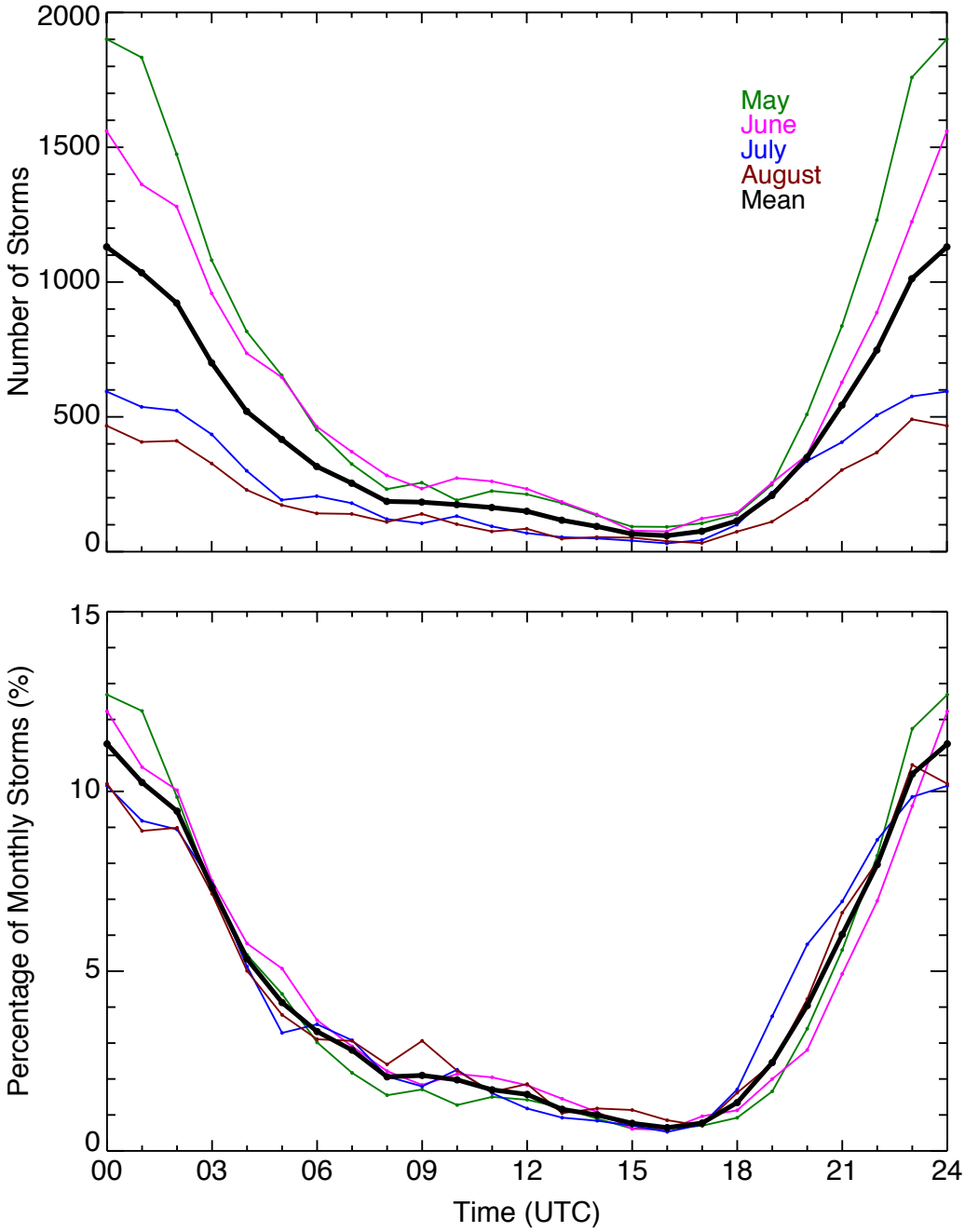

Figure 4.5: Top) climatological diurnal cycle of the number of overshooting storms by month. Bottom) climatological diurnal cycle of the fraction of overshooting storms by month. The bold black line is the 10-year climatological mean.

the shape is nearly identical. There may be a small variation in the fraction of storms that occurs near peak of the diurnal cycle that is related to the amplitude of the diurnal cycle, but this could also be due to the limited sample size of this study.

4.2.1 Geographic Distribution of Overshooting Events

Investigating the distribution of overshooting events is important in diagnosing how these storms form. Figure 4.6 is a map of the number of +2 km storms in each grid box during the entire study period. Because the highest standard NEXRAD elevation angle in convective mode is 19.5°, a radar does not observe the atmosphere within an inverted cone located above the site. Unless the UTLS within that cone is within range of at least three other radars or the reflectivity measurement weight determined by the distance weighting function is sufficient outlined in Homeyer et al. (2014), merged reflectivity data are unavailable there and overshooting echo tops cannot be detected. Therefore, the 'holes' seen on the map are the result of the radar scanning strategy and are not physical. It is very likely that there would be overshooting occurrences in many of those regions.

The vast majority of overshooting events occur in the High Plains and Midwest, with few occurrences east of the Appalachian Mountains or in the southeast. There is evidence of a weak secondary maximum along the east coast. A sharp gradient in the frequency of overshooting exists along a boundary that runs through Texas and Oklahoma, with much more frequent overshooting storms to the west of the boundary. Due to the noisiness of the data it is difficult to tell whether a sharp boundary extends eastward from northeastern Oklahoma. The reason for the boundary in Texas and Oklahoma is not known, although it lies approximately along the typical location of the dry line, which is a frequent triggering mechanism for strong convection.

The maximum echo-top height that occurred in each grid box during the climatology is shown in Figure 4.7. The highest echo-tops are most commonly observed in the southern

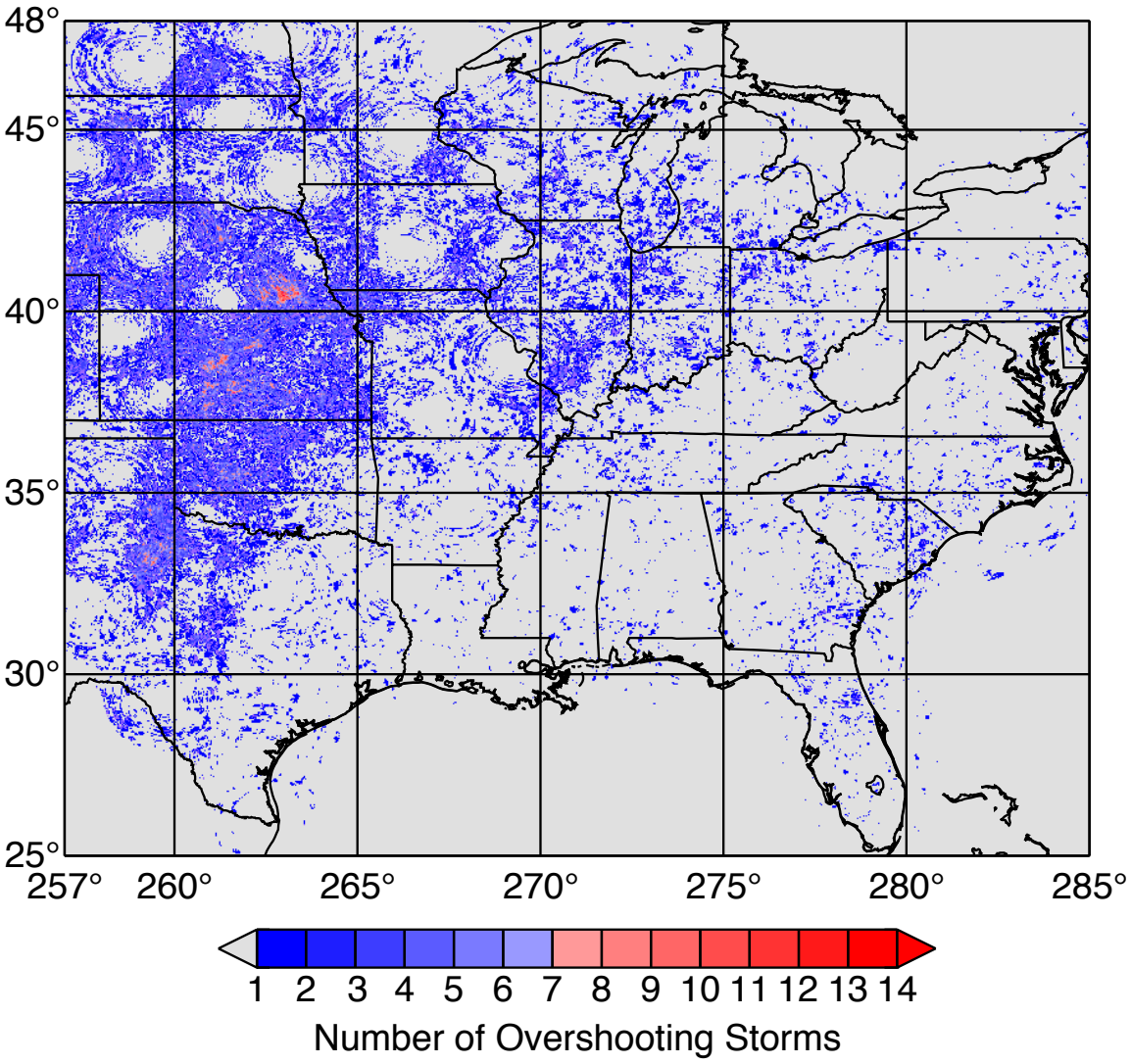

Figure 4.6: Number of instances during the study period that overshooting convection reached at least 2 km above the tropopause in each grid box.

Great Plains. Very few locations south of 35°N have their highest echo-top heights below 16 km. This is due in large part to the fact that in the southern part of the study domain the tropopause generally lies between 13 and 16 km altitude, and convection that does not reach at least 2 km above the tropopause is not included in this analysis. This can be seen more clearly in Figure 4.8, which shows the number of storms within every grid box of the

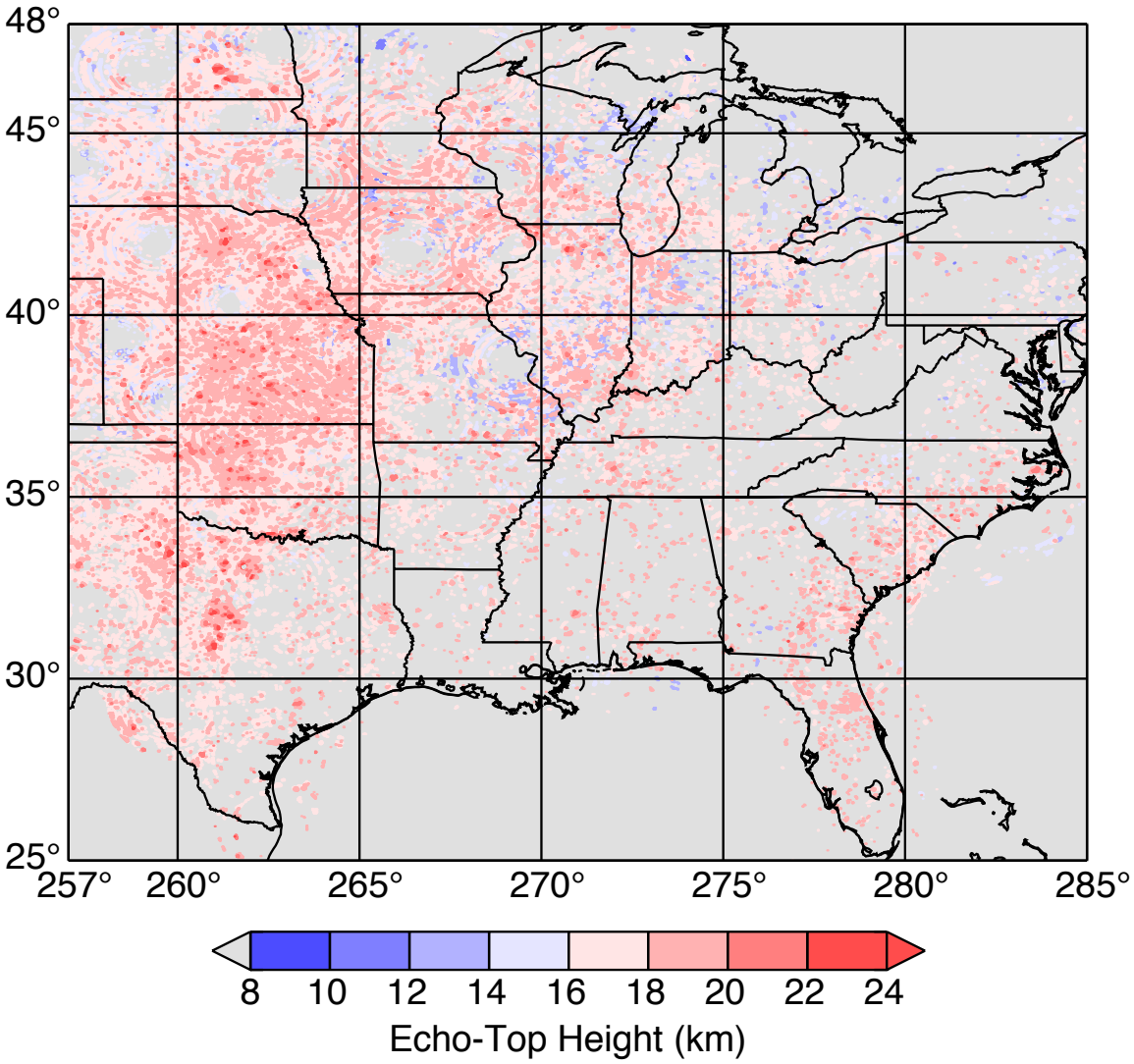

Figure 4.7: Maximum echo-top height observed in each grid box.

domain for each month along with the climatological monthly-averaged tropopause height. As Figure 4.2 demonstrated, overshooting occurrences are most frequent in May when the tropopause heights across the United States are lower than June, July, and August. In the Great Plains, which is the location of the most frequent overshooting storms, the tropopause height typically ranges between 12 and 13 km in May to 15 and 16 km in August. The occurrence of overshooting is also observed to shift northward during the

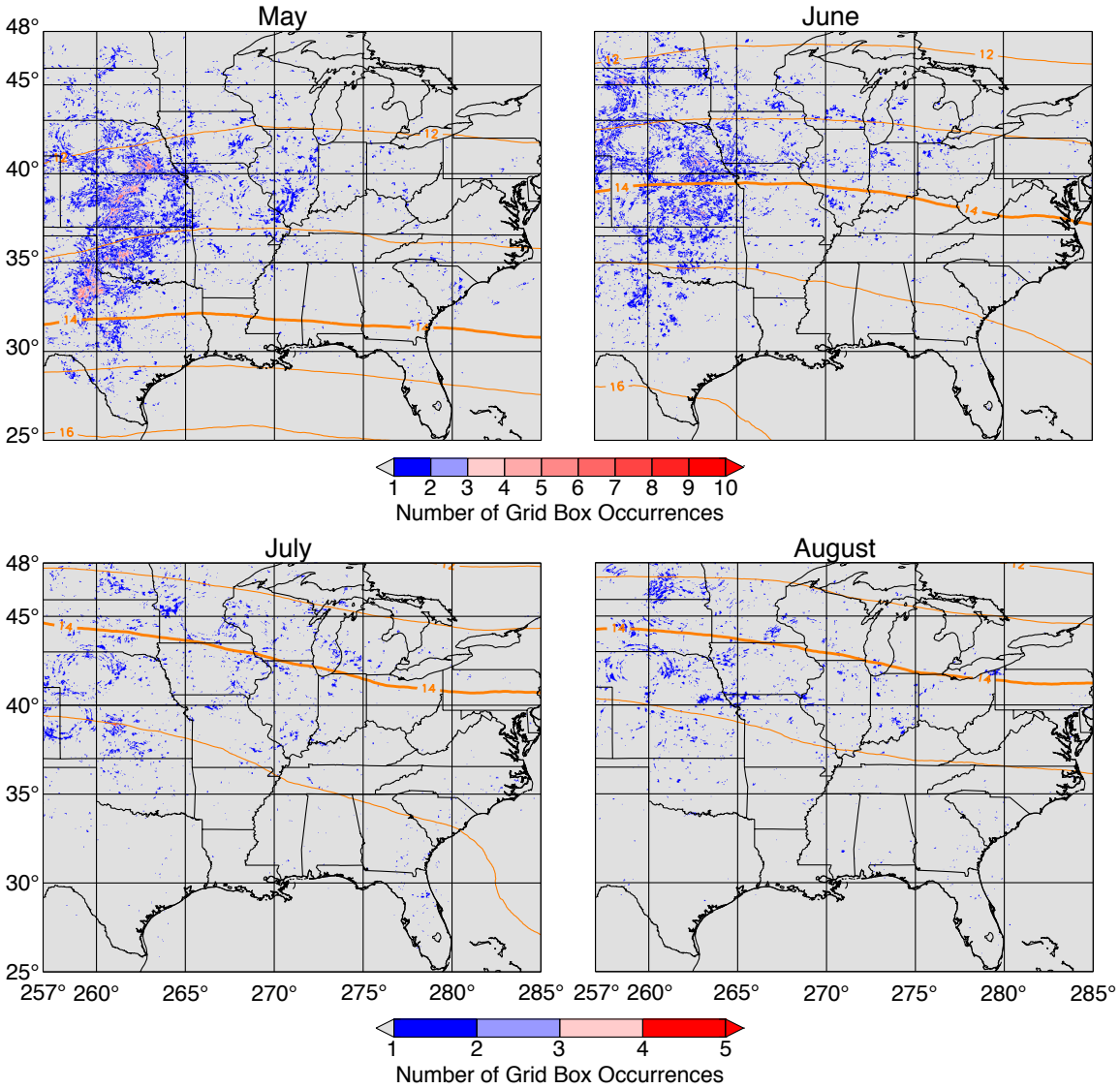

Figure 4.8: Monthly maps of the number of overshooting events in each grid box (shading) and climatological tropopause height (orange contours). For easier comparison, the 14 km contour level is drawn with a heavy line. Note the difference in the color scale between the upper and lower panels.

summer season as the tropopause rises and large-scale dynamical forcing mechanisms weaken.

4.2.2 Vertical Distribution

Figure 4.9 is a graph of the frequency distribution of maximum storm-top altitude for each month. The peak overshooting echo-top height for May and June is between 15 and 16 km. May is the only month that has +2 km storms with maximum echo-top heights below 11 km, although the number of such storms is very small. In July and August, the peak occurrences shift upward to 17 to 18 km. The cumulative fraction is taken from the top-down in order to show the number of storms with maximum echo-tops above certain levels. From using this fraction, we estimate that only approximately 10% of overshooting events contain echo-top heights that exceed 18 km.

In addition to occurring more frequently than during July and August, storms in May and June also reach deeper into the stratosphere, as depicted in Figure 4.10. The histogram for each month is nearly linear, which implies an exponential decrease in the number of storms with increasing height above the tropopause. Although the absolute echo-top heights are generally lower in May and June than in July and August, the overshooting depth tends to be greater, especially in the High Plains where overshooting events occur most frequently (refer back to Figure 4.8). Figure 4.11 is a histogram of the maximum tropopause height overshot by each +2 km storm. The maximum tropopause height of any storm overshooting the tropopause by at least 2 km is 16.8 km. Tropopause heights below 10 km are rare in the mid-latitudes for the MJJA season, so the number of occurrences at these altitudes are correspondingly low. The peak of the histograms shifts upward from 12 km in May to 13 km in June, 14 km in July, and 15 km in August.

4.3 Potential Temperature at the Echo-Top

The echo-top potential temperature is an important quantity for assessing potential transport of overshooting convective air within the stratosphere from North American mid-latitudes to other regions around the globe. Figure 4.12 is a histogram of maximum storm

echo-top potential temperature. Even though the maximum echo-top potential temperature values of the storms are binned into 10 K levels, the effects of the 1 km echo-top height discretization can still be observed. The lowest echo-top potential temperature value calculated is approximately 328 K and the highest value is about 510 K. The cumulative count is taken from the top-down because it provides the number of storms extending above certain theta levels. Over 70% of storms in this study have echo-tops with potential temperature values that are greater than or equal to 380 K. It is important to note that the cumulative fraction would be less if the storms analyzed were not restricted to be 2 km or more above the tropopause. There would be far more storms and the cumulative fraction of high potential temperature values would greatly decrease.

The geographic distribution of the maximum echo-top potential temperature in each grid box for the climatology is shown in Figure 4.13. The high and low echo-top potential temperatures are scattered throughout the map leading us to believe that the distribution of values across the domain does not follow any particular trend.

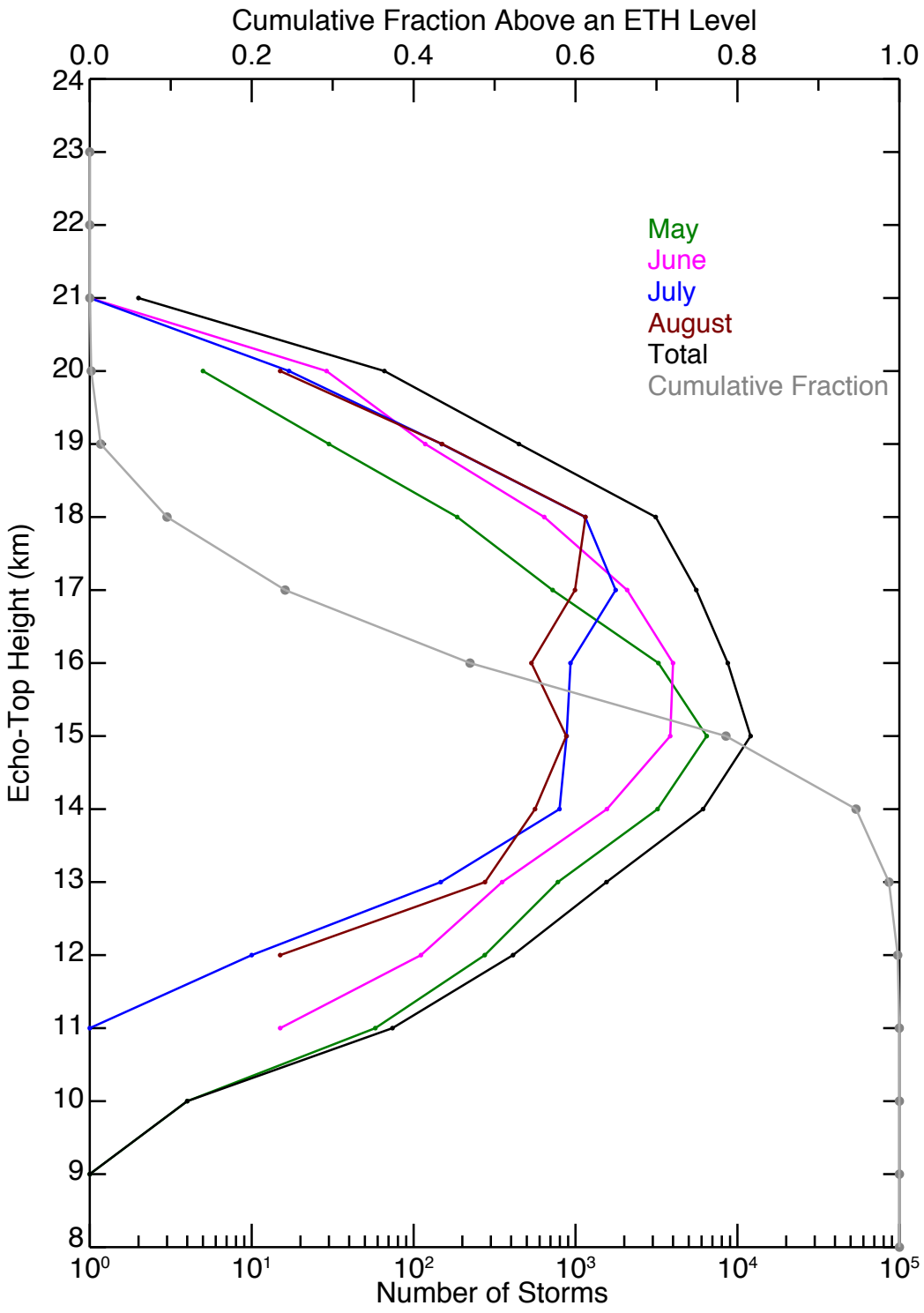

Figure 4.9: Histogram of maximum echo-top height in each storm by month. Bin sizes are 1 km. The histogram for the entire study period is drawn in black. The cumulative fraction of storms, drawn in gray, corresponds to the x-axis at the top of the figure. This fraction is taken from the top, 24 km bin, down.

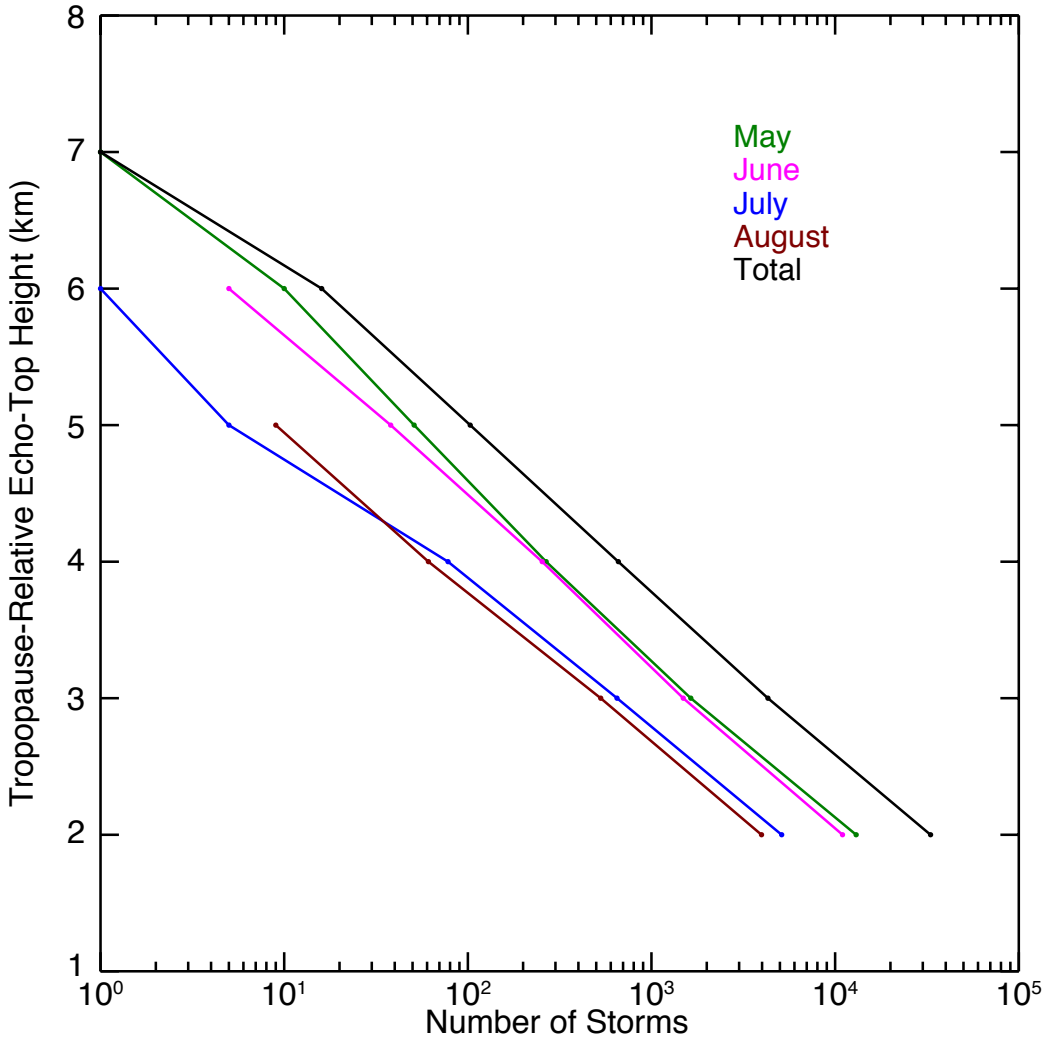

Figure 4.10: Histogram of the monthly storm maximum tropopause-relative echo-top heights. Bin sizes are 1 km. The tropopause-relative echo-top height histogram for the entire study period is drawn in black.

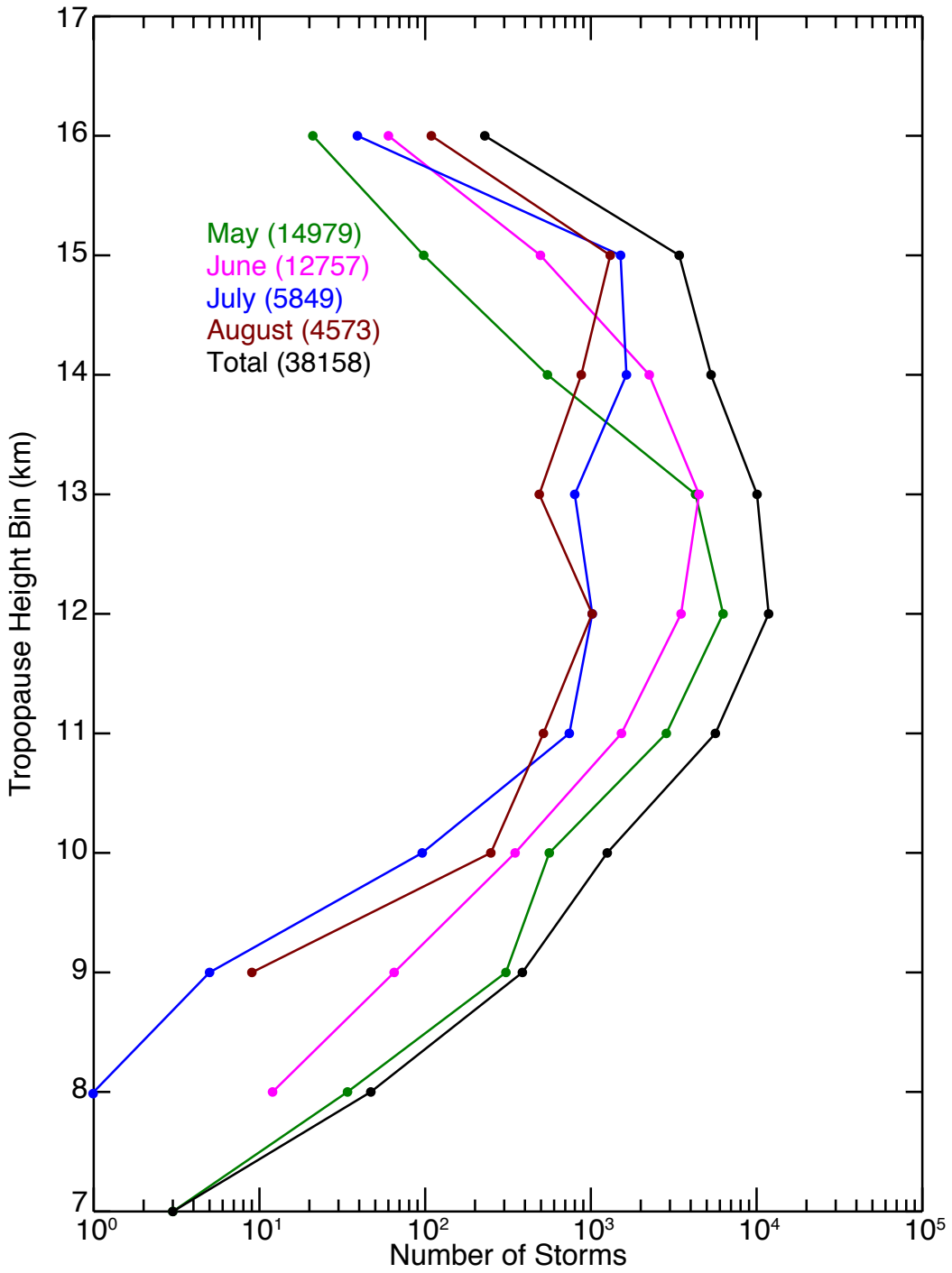

Figure 4.11: Histogram of maximum tropopause heights within an overshooting storm. Bin sizes are 1 km. The total storm tropopause height histogram is drawn in black. The numbers in parenthesis next to the month and total provides the total number of associated events.

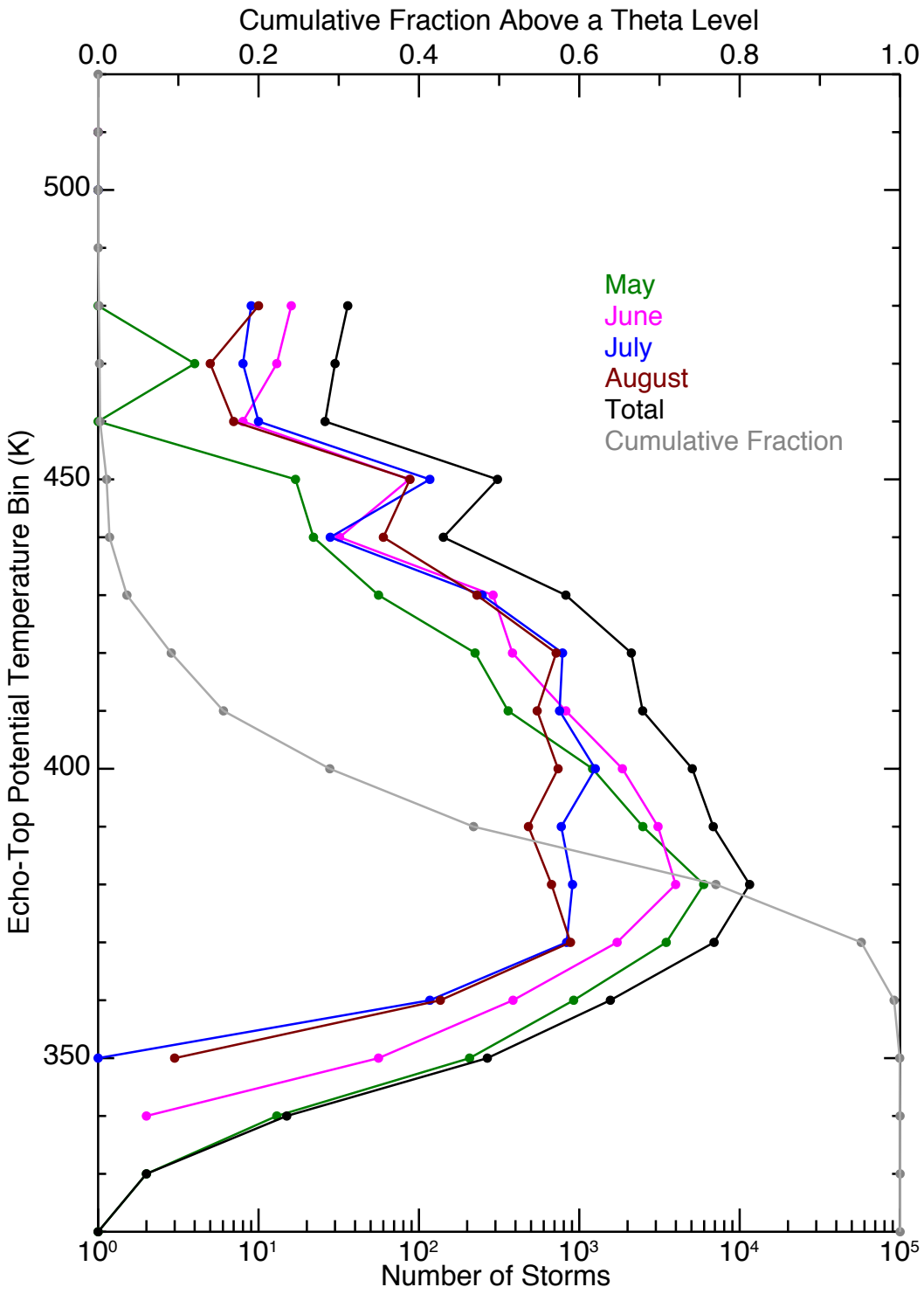

Figure 4.12: Histogram of storm maximum echo-top potential temperature. This plot uses bin sizes of 10 K, starting from 320 K, and counts the number of storms to form each bin. The total bin counts are plotted in black. The cumulative fraction of storms, drawn in gray, corresponds to the x-axis at the top of the figure. This fraction is taken from the top, 510 K bin, down.

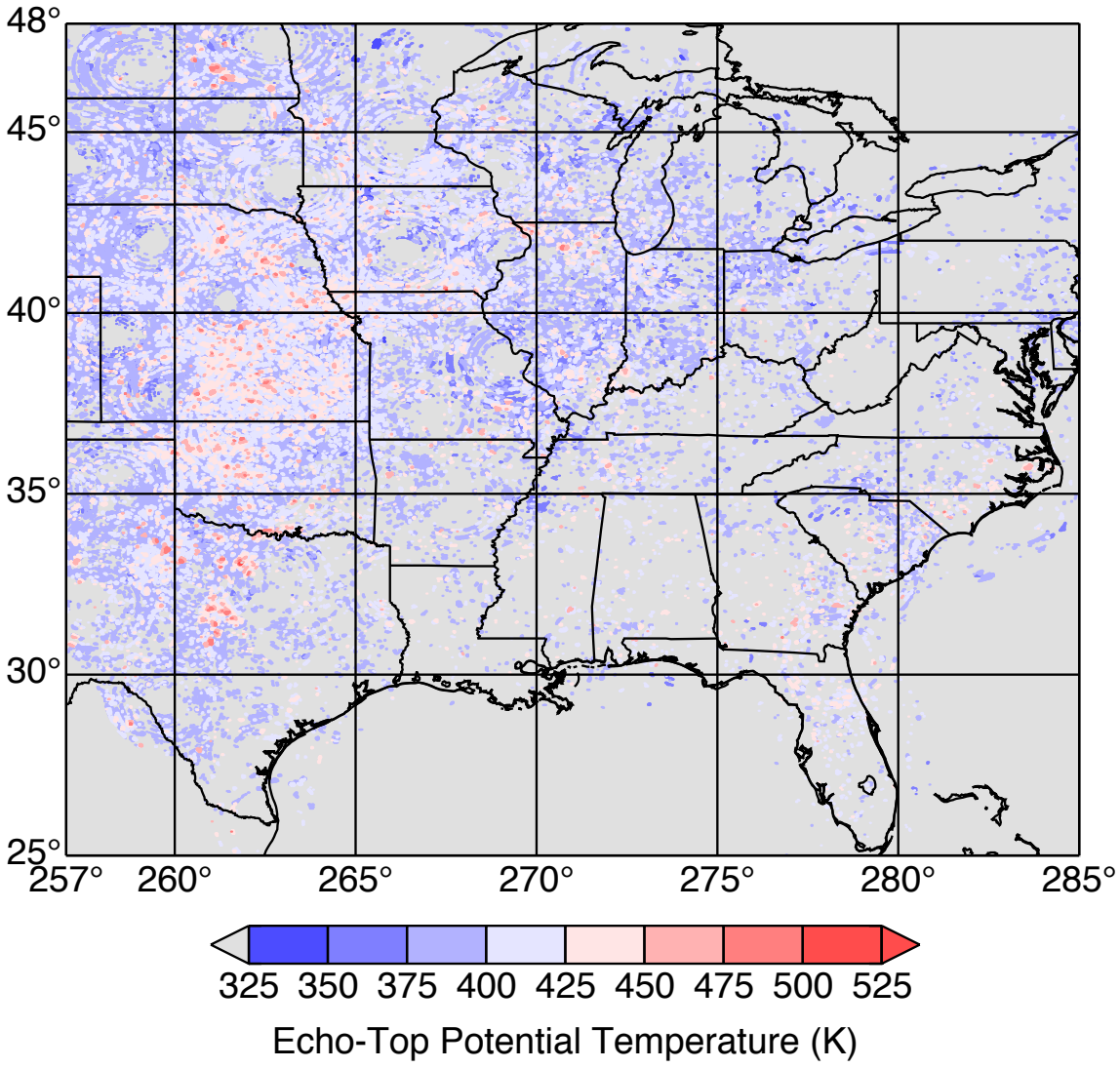

Figure 4.13: Maximum observed echo-top potential temperature for each grid box.

5. SUMMARY AND CONCLUSIONS

This study combines individual WSR-88D radar observations from the NEXRAD network into hourly, high-resolution, three-dimensional, gridded synoptic reflectivity analyses. The reflectivity data are combined with tropopause height estimates from the ERA-Interim reanalysis to create a 10-year dataset of tropopause-overshooting convective events for the May-August period. Using improved quality control procedures and a much longer record, this study expands upon the results in Solomon et al. (2014) and includes an analysis of the interannual variability of overshooting convection over a large part of the continental United States.

Echo-top heights, identified from reflectivity measurements, are compared with the lapse-rate tropopause altitude calculated from ERA-I data, at the same location, to determine overshooting. The quality of the ERA-I tropopause calculations is evaluated by comparisons with tropopause heights calculated from radiosonde observations. The testing shows good agreement between the two datasets with over 88% of tropopause heights calculated from ERA-I data within ± 1 km of radiosonde calculated tropopauses. ERA-I calculations, however, tend to overestimate the tropopause heights compared radiosonde observations. The temperature at altitudes relative to the tropopause from radiosonde observations show a strong tropopause inversion layer (TIL) up to 1-2 km above the tropopause (Birner, 2006; Solomon et al., 2014). Solomon et al. (2014) finds that temperatures from the ERA-Interim are comparable at altitudes >2 km above and >1 km below the tropopause, but at the tropopause ERA-Interim data are biased warm by 2-3 K and underestimate the observed TIL. This results in an overestimation of the tropopause temperature because the tropopause should actually be slightly colder and higher than the data suggests. The impact that overestimating the tropopause height has on the outcome

of this study is unknown but it is important to note that overestimates can lead to large underestimates in the relative altitude of an observed storm (Homeyer, 2014).

In this study, contiguous atmospheric columns that overshoot the ERA-I tropopause by 2 km or more are combined into what we refer to as +2 km storms. After applying the quality control procedures, the number of +2 km storms used in the statistical analysis is 38,158. The number of columns or grid boxes within a single storm ranges from 1 to 1,713 (see Figure 4.1 for the storm size distribution).

During the MJJA period, the highest number of overshooting storms are consistently observed in the month of May (14,979) with the number of events decreasing (on average) each successive month thereafter. The number of storms in May each year is similar to the number observed in June while the number observed in July is similar to August. The frequency of overshooting storms per year varies by about a factor of two with 2011 having the highest number of storms and 2005 the least. The number of events observed in 2004 is slightly below average but overall it is a fairly typical year, lying directly in the middle of the climatology (sixth highest number of storms). The total annual volume of overshooting storms follows the same pattern as the number of storms (2011 highest and 2005 lowest). The year 2004 is a bit anomalous in terms of overshooting volume. The size of the storms (on average) are larger leading to a greater overshoot volume than the occurrences would suggest (fourth highest overshoot volume). Overall though, 2004 is a very typical year and provides a good illustration of the cycles and patterns of overshooting convective storms.

Regardless of month or year, overshooting events have a distinct diurnal cycle. The diurnal cycle of overshooting convection agrees with the results in Solomon et al. (2014). The timing of the peak overshooting occurrences are consistently observed between 22 - 02 UTC (late afternoon to early evening local time) while the fewest overshooting events occur during the middle of the day. The diurnal cycle is similar for the storm area. The timing of overshooting convection maxima is consistent with the times of maximum sum-

mertime precipitation in the U.S. Over the Southeast and the Rockies, both the static instability and the surface convergence favor afternoon moist convection in summer, resulting in very strong late afternoon maxima of precipitation over these regions (Dai et al., 1999).

As noted previously, there is some disagreement in the geographic distribution of tropopause-overshooting occurrences between Solomon et al. (2014) and Bedka et al. (2010). The map provided in Figure 4.6 agrees with the results seen in Solomon et al. (2014), with the vast majority of overshooting convection occurring in the Great Plains region. This is consistent with the maxima of precipitation in the region east of the Rocky Mountains observed in Dai et al. (1999). Overshooting is infrequent east of the Mississippi and in the southeast United States which differs from results in Bedka et al. (2010). The difference in the geographic pattern of tropopause-overshooting convection between the two methods still needs to be investigated further. There is evidence of a weak secondary maximum observed along the east coast. The frequency of events observed in the southern U.S. also decreases with month which coincides with increasing tropopause heights during the MJJA season. Overshooting is uncommon in the southern U.S. in July and August when the average tropopause height is above 15 km. In the high plains region, the tropopause height increases on average from 13 km in May to 15 km in August. Figure 4.8 shows how this increase in the tropopause corresponds to a decrease in the number of occurrences with each successive month for this region.

Regional timing and location of overshooting events is consistent with observed summertime precipitation peaks in the United States. The reason behind the preferential time and location is not fully understood but it is possible that convection is being amplified by the westerly propagation of late afternoon storms that are initiated over the mountains resulting in tropopause-overshooting.

The number of events observed decreases exponentially with height above the tropopause. It is extremely rare to observe storms with echo-top heights that exceed the tropopause by

5 km ($\sim$100 storms). Valid storm echo-top heights are also never found to be greater than 21 km in this study. Storms in May and June frequently extend deeper into the stratosphere than in July and August, but they also typically have lower echo-top heights. Each month has approximately the same fraction of overshooting storms reaching altitude levels above the tropopause. This can be seen in Figures 4.9 and 4.10. From these results, we conclude that the tropopause height plays a vital role in controlling the amount and depth of overshooting convection.

Despite biases in the temperature near the tropopause, the profiles of potential temperature calculated from the ERA-I and radiosonde datasets are nearly indistinguishable (Solomon et al., 2014). The potential temperature at the storm echo-top varies from 328 K to 510 K with no distinct pattern in the geographic distribution of maxima and minima values. The histogram of the cumulative fraction of storm events, provided in Figure 4.12, reveals that over 70% of individual storms have potential temperature values at or above 380 K. This suggests that the impact of overshooting convection over the U.S. could extend well beyond North America and potentially into the tropical lower stratosphere.

REFERENCES

Alcala, C. M. and A. E. Dessler, 2002: Observations of deep convection in the tropics using the Tropical Rainfall Measuring Mission (TRMM) precipitation radar. *J. Geophys. Res.*, **107 (D24)**, 4792, doi:10.1029/2002JD002457.

Bedka, K., J. Brunner, R. Dworak, W. Feltz, J. Otkin, and T. Greenwald, 2010: Objective satellite-based detection of overshooting tops using infrared window channel brightness temperature gradients. *J. Appl. Meteor. Clim.*, **49**, 181–202, doi:10.1175/2009JAMC2286.1.

Berendes, T. A., J. R. Mecikalski, W. M. M. Jr., K. M. Bedka, and U. S. Nair, 2008: Convective cloud identification and classification in daytime satellite imagery using standard deviation limited adaptive clustering. *J. Geophys. Res.*, **113 (D20)**, 207, doi:10.1029/2008JD010287.

Birner, T., 2006: Fine-scale structure of the extratropical tropopause. *J. Geophys. Res. Atmos.*, **111**.

Chagnon, J. M. and S. L. Gray, 2010: A comparison of stratosphere-troposphere transport in convection-permitting and convection-parameterizing simulations of three mesoscale convective systems. *J. Geophys. Res.*, **115**, doi:10.1029/2010JD014421.

Crum, T. D. and R. L. Alberty, 1993: The WSR-88D and the WSR-88D operational support facility. *Bull. Amer. Meteor. Soc.*, **74 (9)**, 1669–1687.

Dai, A., F. Giorgi, and K. E. Trenberth, 1999: Observed and model-simulated diurnal cycles of precipitation over the contiguous United States. *J. Geophys. Res.*, **104 (D6)**, 6577–6402.

Dee, D. P., et al., 2011: The era-interim reanalysis: configuration and performance of the data assimilation system. *Q. J. R. Meteorol. Soc.*, **137 (656)**, 553–597, doi:10.1002/qj.828.

Dessler, A. E., 2002: The effect of deep, tropical convection on the tropical tropopause layer. *J. Geophys. Res.*, **107 (D3)**, 4033, doi:10.1029/10.1029/2001JD000511.

Dessler, A. E. and S. C. Sherwood, 2004: Effect of convection on the summertime extratropical lower stratosphere. *J. Geophys. Res.*, **109 (D23)**, 301, doi:10.1029/2004JD005209.

Gettelman, A., P. Hoor, L. L. Pan, W. J. Randel, M. I. Hegglin, and T. Birner, 2011: The extratropical upper troposphere and lower stratosphere. *Rev. Geophys.*, **49**, RG3003, doi:10.1029/2011RG000355.

Gettelman, A., M. L. Salby, and F. Sassi, 2002: Distribution and influence of convection in the tropical tropopause region. *J. Geophys. Res.*, **107 (D10)**, 4080, doi: 10.1029/2001JD001048.

Gray, S. L., 2003: A case study of stratosphere to troposphere transport: The role of convective transport and the sensitivity to model resolution. *J. Geophys. Res.*, **108 (D18)**, 4590, doi:10.1029/2002JD003317.

Holton, J. R., P. H. Haynes, M. E. McIntyre, A. R. Douglass, R. B. Rood, and L. Pfister, 1995: Stratosphere-troposphere exchange. *Rev. Geophys.*, **33**, 403–439, doi:10.1029/95RG02097.

Homeyer, C. R., 2014: Formation of the Enhanced-V infrared cloud top feature from high-resolution three-dimensional radar observations. *J. Atmos. Sci.*, **71**, 332–348, doi: 10.1175/JAS-D-13-079.1.

Homeyer, C. R. and K. P. Bowman, 2013: Rossby wave breaking and transport between the tropics and extratropics above the subtropical jet. *J. Atmos. Sci.*, **70 (2)**, 607–626, doi:10.1175/JAS-D-12-0198.1.

Homeyer, C. R. and M. R. Kumjian, 2014: Microphysical characteristics of overshooting convection from polarimetric radar observations. *J. Atmos. Sci.*, **in press**, doi:10.1175/JAS-D-13-0388.1.

Homeyer, C. R., L. L. Pan, and M. C. Barth, 2014: Transport from convective overshooting of the extratropical tropopause and the role of large-scale lower stratosphere stability. *J. Geophys. Res. Atmos.*, **119**, 2220–2240, doi:10.1002/2013JD020931.

Lakshmanan, V., T. Smith, K. Hondl, G. J. Stumpf, and A. Witt, 2006: A real-time, three-dimensional, rapidly updating, heterogeneous radar merger technique for reflectivity, velocity, and derived products. *Wea. Forecasting*, **22**, 802–823.

Langston, C., J. Zhang, and K. Howard, 2007: Four-dimensional dynamic radar mosaic. *J. Atmos. Oceanic Technol.*, **24**, 776–790, doi:10.1175/JTECH2001.1.

Lindsey, D. T. and L. Grasso, 2008: An effective radius retrieval for thick ice clouds using GOES. *J. Appl. Meteor. Climatol.*, **47**, 1222–1231.

NWS, 2016: Maps of the nws rawinsonde network. URL `http://www.ua.nws.noaa.gov/nws_upper.htm`.

Rosenfeld, D., W. L. Woodley, A. Lerner, G. Kelman, and D. T. Lindsey, 2008: Satellite detection of severe convective storms by their retrieved vertical profiles of cloud particle effective radius and thermodynamic phase. *J. Geophys. Res.*, **113 (D04)**, 208, doi:10.1029/2007JD008600.

Ruzanski, E. and V. Chandrasekar, 2012: An investigation of the short-term predictability of precipitation using high-resolution composite radar observations. *J. App. Met. Clim.*, **51**, 912–925, doi:10.1175/JAMC-D-11-069.1.

Solomon, D. L., K. P. Bowman, and C. R. Homeyer, 2014: Tropopause-penetrating convection from three-dimensional gridded NEXRAD data. *J. Atmos. Sci.*, submitted.

Stohl, A., H. Wernli, P. James, M. Bourqui, C. Forster, M. A. Liniger, P. Seibert, and M. Sprenger, 2003: A new perspective of stratosphere-troposphere exchange. *Bull. Amer. Meteor. Soc.*, **84**, 1565–1573, doi:10.1175/BAMS-84-11-1565.

Wang, P. K., 2003: Moisture plumes above thunderstorm anvils and their contributions to cross-tropopause transport of water vapor in midlatitudes. *J. Geophys. Res.*, **108 (D6)**, doi:10.1029/2002JD002581.

WMO, 1957: Meteorology - a three-dimensional science: Second session of the commision for aerology. *WMO Bulletin*, **IV (4)**, 134–138.

Zhang, J., K. Howard, and J. J. Gourley, 2005: Constructing three-dimensional multiple-radar reflectivity mosaics: Examples of convective storms and stratiform rain echoes. *J. Atmos. Oceanic Technol.*, **22**, 30–42.

Zhang, J., S. Wang, and B. Clarke, 2004: WSR-88D reflectivity quality control using horizontal and vertical reflectivity structure. *Proceedings of IIth Conference on Aviation, Range and Aerospace Meteorology*, **1**, 5–6.

Zhang, J., et al., 2011: National mosaic and multi-sensor QPE (NMQ) system: Description, results, and future plans. *Bull. Amer. Meteor. Soc.*, **92**, 1321–1338, doi: 10.1175/2011BAMS-D-11-00047.1.